iScience

CellPress
OPEN ACCESS

Article

Dioxygen Activation by Internally Aromatic Metallacycle: Crystallographic Structure and Mechanistic Investigations

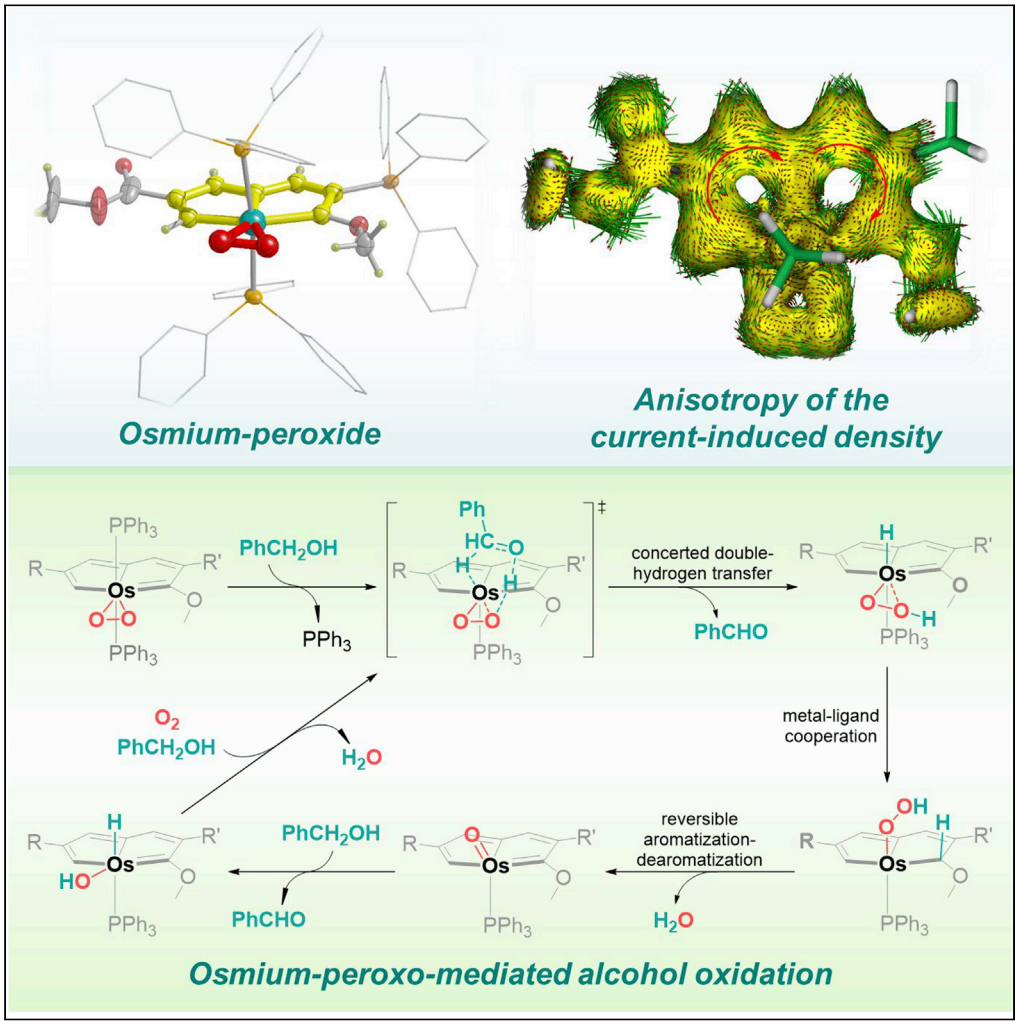

Zhihong Deng, Peng Wu, Yapeng Cai, ..., Hong Zhang, Binju Wang, Haiping Xia

wangbinju2018@xmu.edu.cn (B.W.)
hpxia@xmu.edu.cn (H.X.)

HIGHLIGHTS

A dioxygen-derived mononuclear osmium-peroxo complex was characterized

The peroxo ligand is stabilized by internally aromatic metallacycle

O_2 activation involves the reversible aromatization-dearomatization

A concerted double-hydrogen transfer mechanism for alcohol dehydrogenation

Deng et al., iScience 23, 101379
August 21, 2020
https://doi.org/10.1016/j.isci.2020.101379

iScience

CellPress
OPEN ACCESS

Article

Dioxygen Activation by Internally Aromatic Metallacycle: Crystallographic Structure and Mechanistic Investigations

Zhihong Deng,[1,3] Peng Wu,[1,3] Yapeng Cai,[1] Yanheng Sui,[1] Zhixin Chen,[1] Hong Zhang,[1] Binju Wang,[1,*] and Haiping Xia[1,2,4,*]

SUMMARY

Mononuclear metal-peroxo species are invoked as the key intermediates in metalloenzymatic or synthetic catalysis. However, either transience or sluggishness reactivity of synthetic analogs of metal-peroxo species impedes our understanding of oxygen activation mechanism. Herein, we designed and characterized a dioxygen-derived mononuclear osmium-peroxo complex, in which the peroxo ligand is stabilized by internally aromatic metallacycle. We demonstrate that the osmium-peroxo species shows catalytic activity toward promoterless alcohol dehydrogenations. Furthermore, computational studies provide a new mechanism for the osmium-peroxo-mediated alcohol oxidation, starting with the concerted double-hydrogen transfer and followed by the generation of osmium-oxo species. Interestingly, the internally aromatic metallacycle also plays a vital role in catalysis, which mediates the hydrogen transfer from osmium center to the distal oxygen atom of Os–OOH moiety, thus facilitating the Os–OOH→Os=O conversion. We expect that these insights will advance the development of aromatic metallacycle toward aerobic oxidation catalysis.

INTRODUCTION

Capturing highly active species and illustrating their reactivities are central issues in dioxygen activation chemistry (Elwell et al., 2017; Karlin, 2010; Lewis and Tolman, 2004; Hong et al., 2017; Dong at al., 2013; Solomon et al., 2014; Cho et al., 2016). Mononuclear metal-peroxo complexes are commonly implicated as reactive intermediates in oxidative catalysis of enzymatic or abiological systems, and considerable efforts have been dedicated to the synthesis and the mechanistic studies of them (Meunier, 2000; Karlsson, 2003; Yee and Tolman, 2015; Nam, 2015; Quist et al., 2017; Costas et al., 2004). Despite the fact that a number of mononuclear metal-peroxides have been elegantly synthesized and characterized, either the transient nature or the sluggish reactivity of these intermediates hampers our insight into the detailed dioxygen activation mechanisms during catalytic turnover (Shook et al., 2008; Cho et al., 2011; Ohta et al., 2013; Barman et al., 2019; Tronic et al., 2011). As the relative reactivity and stability of the metal-oxygen species are highly dependent on the supporting ligands or coordination environments (Cook and Borovik, 2015; Kovacs, 2015; Neu et al., 2015; Yan Poon et al., 2019), the rational ligand design constitutes a promising way to tune the relative stability and reactivity of metal-peroxo complexes (Mirica et al., 2004; Baglia et al., 2017). Internally aromatic metallacycles, featured by a rigid C^C^C-tridentate framework with electronically delocalized metallacyclic cores (Zhuo et al., 2019), were demonstrated to be efficient in stabilizing various metallacycle derivatives (Zhu et al., 2015). Structurally, these derivatives are termed as "carbolong complexes," due to their unique ring systems consisting of different number of carbon atoms and one metal center in the equatorial plane (Zhu and Xia, 2018). Inspired by these findings, we speculated that internally aromatic metallacycle could be an ideal framework for oxygen binding and activation, which ultimately enable us to characterize a stable metal-dioxygen intermediate and further study its catalytic transformations.

Oxidation of alcohols toward corresponding carbonyl compounds is a fundamentally important reaction in both laboratory and industry (Kopylovich et al., 2015). However, the conventional alcohol oxidations usually require stoichiometric inorganic oxidants, in which a large amount of toxic waste was generated (Tojo and Marcos, 2006). As a result, developing environmentally benign catalytic systems using molecular oxygen as

[1]College of Chemistry and Chemical Engineering, Xiamen University, Xiamen 361005, China

[2]Shenzhen Grubbs Institute, Department of Chemistry, Southern University of Science and Technology, Shenzhen 518055, China

[3]These authors contributed equally

[4]Lead Contact

*Correspondence: wangbinju2018@xmu.edu.cn (B.W.), hpxia@xmu.edu.cn (H.X.)

https://doi.org/10.1016/j.isci.2020.101379

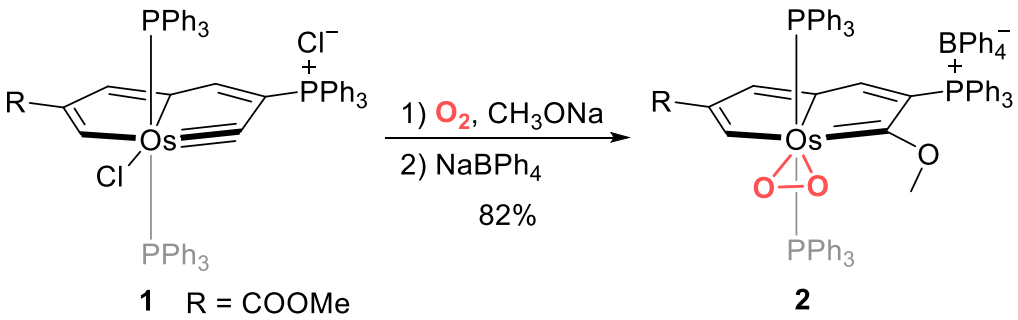

Scheme 1. Synthesis of 2 via the Reaction of Osmapentalyne 1 with O_2 in the Presence of CH_3ONa
See also Figures S1 and S14–S16.

terminal oxidant is one of the long-term pursuit of chemists (Arends and Sheldon, 2004; Parmeggiani and Cardona, 2012; Shi et al., 2012; Punniyamurthy et al., 2005). Although great progress has been achieved in transition-metal-catalyzed aerobic oxidations of alcohols in the past decades (Brink et al., 2000; Stahl, 2004, 2005; Ryland and Stahl, 2014; Chung et al., 2013; Konnick, and Stahl, 2008; Sigman and Jensen, 2006), examples of alcohol oxidation mediated by mononuclear metal-peroxo species are rare (Bianchini et al., 1990; Esteruelas et al., 2011). Interestingly, osmium-dioxygen adduct was found to be an active catalyst in alcohol oxidations (Esteruelas et al., 2011). Nevertheless, understanding on the structural and mechanistic features in osmium-dioxygen-mediated alcohol oxidation is still limited.

Herein, we present the synthesis, characterization, and reactivity of a mononuclear osmium-peroxo complex. Theoretical investigations, including aromatic stabilization energy (ASE), nucleus-independent chemical shift (NICS) and anisotropy of the current-induced density (ACID), as well as experimental evidences indicated that the active species was stabilized by the internally aromatic pincer backbone. In particular, we demonstrate that the osmium-peroxo species could act as a pre-catalyst in alcohol oxidations without using additives. In contrast to the commonly proposed β-hydride elimination mechanisms for alcohol oxidation, our calculations show a new mechanism that the osmium-peroxo-catalyzed aerobic oxidation of alcohol proceeds via the concerted double-hydrogen transfer. As far as we know, the result outlined above is the first experimental evidence of a structurally characterized mononuclear metal-peroxide that is able to perform the alcohol dehydrogenation.

RESULTS AND DISCUSSION

Synthesis and Characterization of an Osmium-Peroxo Complex

Osmapentalyne **1** (Zhu et al., 2013) was used as the starting material to study the binding of dioxygen (Scheme 1). The nucleophilic attack at carbyne carbon atom by sodium methoxide led to the reduction of metal center and dissociation of chloride, which facilitated the coordination and the following reduction of dioxygen. The yellow solution of **1** and CH_3ONa in methanol under dioxygen atmosphere at room temperature (RT) underwent gradual color change to generate a brown solution (Figure 1A, left insets), which was followed by ultraviolet-visible spectroscopic changes (Figure 1A). As also indicated by *in situ* NMR, the mixture of **1** and excess CH_3ONa in the presence of dioxygen at RT for 3 h resulted in almost quantitative conversion to **2** (Figure S1, and see also Transparent Methods for details), which was characterized by high-resolution electrospray ionization-mass spectroscopy (HRMS). The HRMS of **2** shows a prominent peak at *m/z* = 1,187.2762 (Figure 1B), in which the mass and isotope distribution patterns correspond to the cation of **2** (calculated for cation of **2**, *m/z* 1.187.2793). Upon introduction of ^{18}O into **2** using $^{18}O_2$, a shift of four mass units was observed, from *m/z* 1,187.2762 to 1,191.2884 (Figure 1B, insets), indicating that dioxygen bound to the metal center of **2**.

The good thermal stability of **2** (Figure S2) in the absence of substrates allowed us to obtain single crystals suitable for spectroscopic and structural analysis. The solid infrared spectrum (KBr) of **2** exhibits a vibrational band at 913 cm^{-1}, which shifts to 860 cm^{-1} upon replacement of ^{16}O by ^{18}O (Figure 1C). The observed isotopic shift value of $\Delta\nu$ = 53 cm^{-1} is consistent with the value of 52 cm^{-1}, calculated using Hooke's law of harmonic oscillators. These values are also comparable to those recorded for metal-peroxo

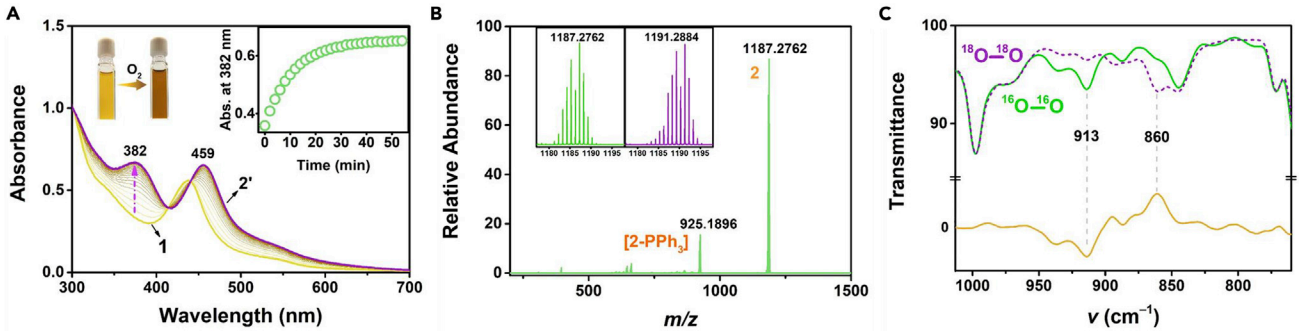

Figure 1. Spectroscopic Characterization of 2

(A) UV-visible spectral changes observed upon addition of CH_3ONa (15 equiv; 1.5 mM in methanol) to a methanol solution of **1** (0.1 mM; yellow line) under O_2 atmosphere at RT. The left insets show the color changes of the solution during the conversion of **1** (yellow) to **2′** (brown). The right inset shows the change over time of the absorbance at 382 nm.

(B) High-resolution electrospray ionization mass spectrometry spectra (positive ion mode) of the reaction mixture of **1** and CH_3ONa (5 equiv, CH_3OH, 3 h) in air. The insets show the observed isotope distribution patterns for **2**-$^{16}O_2$ (green panel) and labeled **2**-$^{18}O_2$ (purple panel).

(C) Fourier transform infrared spectra of **2**-$^{16}O_2$ (green line) and **2**-$^{18}O_2$ (purple dashed line) as recorded from KBr disks. Yellow line is the difference spectrum of **2**-$^{16}O_2$ and **2**-$^{18}O_2$.

See also Figure S17.

complexes (Cho et al., 2011; Tronic et al., 2011; Hu et al., 2004; Lee et al., 2012; Waidmann et al., 2010), and lead us to conclude that the O_2 unit in **2** possesses a peroxo character.

Direct evidence for the geometry of osmium-dioxygen moiety is provided by the X-ray crystal structure of **2**. As shown in Figure 2, the crystal structure revealed a mononuclear osmium complex with the triangular Os−O_2 unit having a small bite angle (40.18(14)º for O1−Os−O2). The five coordination sites in the equatorial plane are occupied by the C^C^C-type tridentate ligand and the peroxo ligand, and the axial positions are occupied by two phosphine ligands. The peroxo ligand within the Os−O_2 unit is bound almost symmetrically to the metal center with Os−O bond lengths of 2.034(4) and 2.051(4) Å. The O1−O2 bond length in **2** (1.403(5) Å) is within the range of O−O bond distances found in other osmium-peroxo complexes (*ca.* 1.396–1.452 Å) (Mezzetti et al., 1994; Maddock et al., 1996). In accordance with the experimental values, we concluded that **2** is a side-on osmium-peroxo complex. This structure contains three metal-carbon bonds and two metal-oxygen bonds in an equatorial plane, which has not been reported previously in coordination chemistry. To the best of our knowledge, this crystal structure is the first example of a metal-peroxo complex lacking heteroatomic binding sites of a polydentate ligand scaffold.

Aromaticity Evaluation of Osmium-Peroxo Complex

Aromaticity plays vital role in stabilizing organic-aromatic or metalla-aromatic compounds (Krygowski and Cyrański, 2001; Chen and Jia, 2013; Schleyer, 2001). In this study, the stability of the osmium-peroxo complex **2** could be attributed to the aromaticity of the metallacycle composed of the C^C^C skeleton and a metal center, which is also thought to have strong influence on the oxygen transfer process. The good stability, ring planarity, bond length equalization, and low-field exocyclic proton chemical shifts of metallacycle indicate that complex **2** is aromatic in nature. To shed light on the aromaticity, density functional theory (DFT) calculations were performed on the simplified model complexes **2-1** and **2-2**. The PPh_3 and the ester in **2-1** are replaced by PH_3 and methyl, respectively, whereas in **2-2**, the ester group is reserved (Figure 3). The computed positive ASE values (Schleyer and Pühlhofer, 2002; Wannere et al., 2003) and negative NICS values (Schleyer et al., 1996; Chen et al., 2005; Fallah-Bagher-Shaidaei et al., 2006) generally act as the indicator for aromaticity. As depicted in Figure 3A the ASE values of **2-1** (28.7 and 25.8 kcal mol^{-1}) are comparable to the corresponding ASE values of previously reported metalla-aromatics (Chen and Jia, 2013; Landorf and Haley, 2006; Fernández et al., 2015), indicating the aromaticity of **2**. The calculated $NICS(1)_{zz}$ values for the two metallacyclic rings of **2-2** are −10.3 (ring a) and −12.7 (ring b) ppm (Figure 3B), which are similar to those reported for other metalla-aromatics (Wei et al., 2018; Frogley and Wright, 2018). The aromaticity of **2** is further supported by the ACID (Herges and Geuenich, 2001; Geuenich et al., 2005), which can simulate the density and direction of the induced ring current in a molecular system under an external magnetic field. As shown in Figure 3C, an obvious clockwise diatropic ring current can be observed in **2-2**, indicating the aromaticity of the two fused five-membered rings.

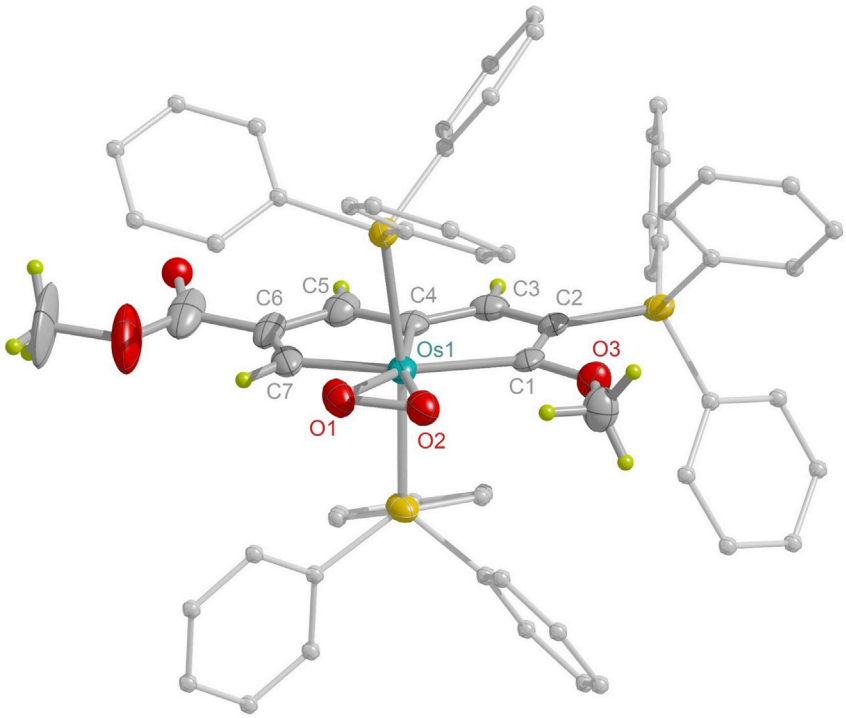

Figure 2. Molecular Structure of the Cation of 2

Molecular structure of **2** with thermal ellipsoids drawn at 50% probability level. Hydrogen atoms in the PPh_3 moieties are omitted for clarity. Selected bond lengths (Å) and angles (deg): O1−O2 1.403(5), Os1−O1 2.034(4), Os1−O2 2.051(4), O1−Os1−O2 40.18(14), Os1−O1−O2 70.6(2), Os1−O2−O1 69.2(2).
See also Table S1.

The Reactivity of Osmium-Peroxo Complex in the Catalytic Oxidation of Alcohol

Metal-oxygen intermediate was extensively invoked as the active species for the hydrogen atom abstraction from C−H or O−H bonds (Sacramento and Goldberg, 2018; Gordon et al., 2019). As such, we first investigated the catalytic activity of **2** with 4-methylbenzyl alcohol using pure oxygen as the terminal oxidant. It is seen from Figure 4 that the catalytic oxidation completes within 12 h, affording the desired aldehyde in 92% isolated yield. With the preliminarily optimal reaction conditions in hand, we explored the substrate generality of this protocol (Figure S3). We found that alcohols with weak C-H bonds and acidic O-H bonds, such as 4-nitrobenzyl alcohol, 1-pyrenemethanol, and benzhydrol, were converted to the corresponding carbonyl compounds in high yield. In contrast, cyclohexanol with stronger C-H bond and slightly acidic O-H bond had significantly low yield relative to benzylic alcohols, suggesting that the alcohol oxidation rate is dependent on the C-H strength of substrate (Rajabimoghadam et al., 2018).

The parallel kinetic isotope effect (KIE) studies conducted with the **2**-catalyzed oxidation of 4-$MeC_6H_4CH_2OH$ (**3**) and 4-$MeC_6H_4CH_2OD$ (**3-OD**), respectively, revealed an overall KIE value of 1.16 (Figures 4A and S4). In addition, with **3** and 4-$MeC_6H_4CD_2OH$ (**3-CD_2**), a relatively larger overall KIE value of 2.50 was observed (Figures 4B and S5). To ensure the reliability of the later KIE value, intermolecular competition experiment by mixing equal molar amounts of **3** and **3-CD_2** in the same reaction vessel was carried out to give an overall KIE value of 2.86 (Figure S6). The aforementioned kinetic results imply that the bond cleavage is C−H rather than O−H occurring in the turnover-limiting step (Simmons and Hartwig, 2012; Jones, 2003).

Mechanistic Studies of Catalytic Oxidation

Despite extensive experimental studies, the mechanisms of O_2 activation and the metal-peroxo-mediated oxidation of alcohols remain elusive. Herein, computational studies in combination with experiments were conducted to gain insight into the detailed mechanism. We first carried out the catalytic oxidation reaction

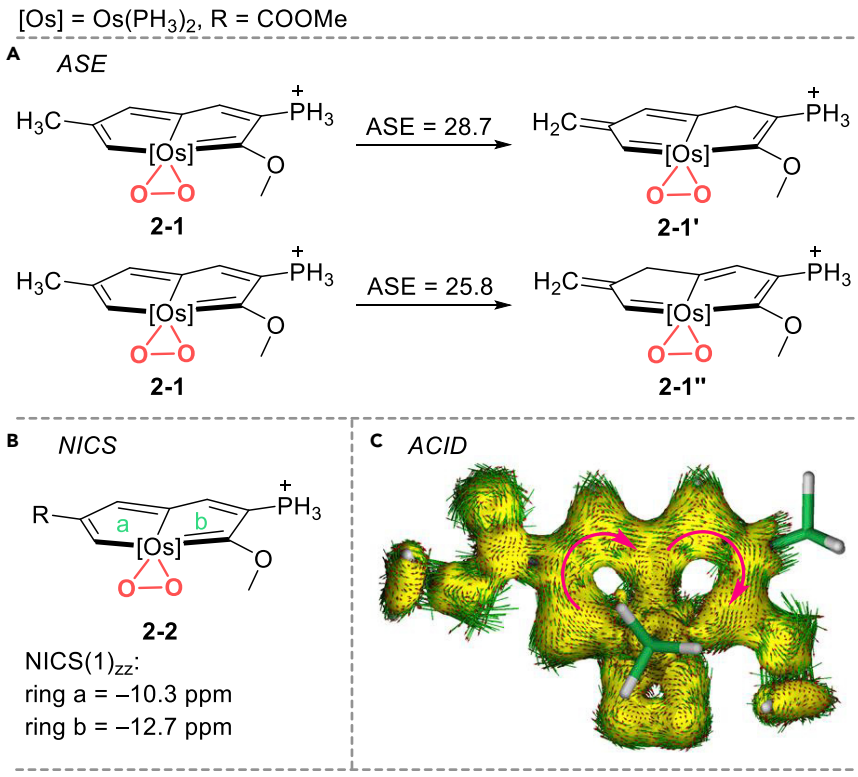

Figure 3. Aromaticity Evaluation of 2

(A) Aromatic stabilization energy (ASE, kcal mol^{-1}) evaluations of the aromaticity of model complex **2-1**.

(B) $NICS(1)_{zz}$ (nucleus-independent chemical shift along the z axis at 1 Å above the ring critical point) evaluations of the aromaticity of model complex **2-2**.

(C) Anisotropy of the current-induced density (ACID) plot of **2-2** from π contribution with an isosurface value of 0.035. The magnetic field vector is orthogonal to the ring plane and is directed upward (aromatic species exhibit clockwise diatropic circulations).

with excess of 1,1-diphenylethylene and 2,4,6-tri-tert-butylphenol, respectively, and found that free radical scavenger did not obviously suppress the reaction rates and the yield of aldehyde. This finding suggests that the catalytic oxidation probably proceeds via a non-radical mechanism. In the control experiments, the amounts of PPh_3 and $Ph_3P{=}O$ in the initial stage of the reaction mixture with and without substrate were monitored by gas chromatography-mass spectrometry (GC-MS) (Figure S7). It was found that the amount of free PPh_3 in both control experiments were negligible, but the amount of $Ph_3P{=}O$ in the initial stage of the reaction mixture in the presence of substrate was about 11 mg according to the GC-MS analysis. As such, we think that the first step of the catalytic cycle involves the dissociation of one of the phosphine ligand, which was then oxidized to phosphine oxide. In addition, the addition of PPh_3 would significantly suppress the catalytic reaction, probably due to the inhibition of first step in catalytic cycle or competitive oxidation between PPh_3 and substrate. With these results, we proposed that the first step of catalysis involves the dissociation of one PPh_3 ligand from **2** and the following alcohol coordinate to the metal center (Figure S8). Figure 5 presents the calculated free energy profiles for the osmium-peroxo-catalyzed aerobic oxidation of alcohols. It is seen from Figure 5 that two distinct binding conformations of benzyl alcohol can be located in this study. In reactant complex **RC0**, the hydroxyl oxygen atom is coordinated to osmium center, whereas in the alternative reactant complex **RC1**, the hydrogen of hydroxyl is H-bonded to one of the peroxo oxygen atom. Although **RC0** is calculated to be 8.6 kcal/mol lower in energy than **RC1**, the aldehyde formation via the initial proton transfer from the hydroxyl group of substrate to the peroxo moiety in **RC0**, followed by another hydride dissociation from the benzylic C–H bond, is demonstrated to be highly unfavorable (the calculated barriers are over 30 kcal/mol in all three possible pathways, see Figure S9). By contrast, we located a new pathway from **RC1** (Figure 5), in which the proton transfer from the hydroxyl group to the peroxo moiety is coupled with the hydride transfer from the benzylic

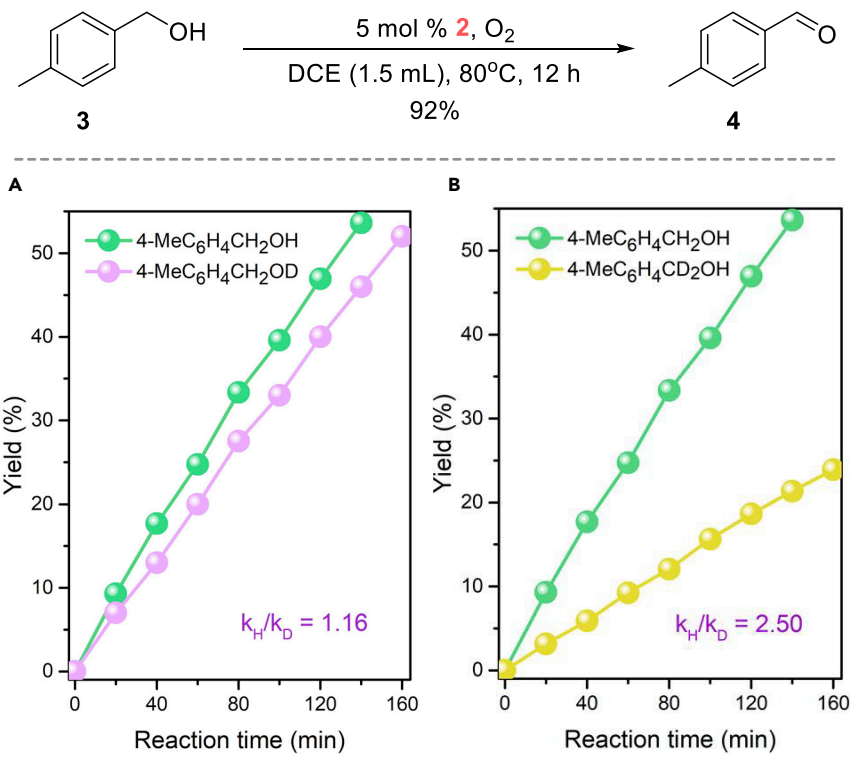

Figure 4. Aerobic Catalytic Oxidation of *p*-methylbenzyl Alcohol by 2 and the Kinetic Isotope Effects

(A) Parallel KIE studies conducted for the **2**-catalyzed oxidation of 4-$MeC_6H_4CH_2OH$ (**3**) and isotopically labeled 4-$MeC_6H_4CH_2OD$ (**3-OD**). (B) Parallel KIE studies conducted for the **2**-catalyzed oxidation of 4-$MeC_6H_4CH_2OH$ (**3**) and 4-$MeC_6H_4CD_2OH$ (**3-CD_2**).

See also Figures S3–S6.

CH_2 group to metal center (**TS1**). This new reaction channel involves a Gibbs energy barrier of 22.1 kcal/mol relative to **RC0**, leading to the formation of aldehyde products and OsH(OOH) species in **IC1**. By investigating all the possible reaction pathways for the OsH(OOH) intermediate in **IC2** (Figure S10), we found that the most favorable pathway is initiated by the hydride shift from osmium center to the neighboring C1 (**TS2**), with a Gibbs energy barrier of 16.1 kcal/mol relative to **IC2**, whereas the hydride transfer to the another neighboring carbon (C7) requires an even higher barrier of 20 kcal/mol (Figure S11). Notably, conversion of **IC2** to **IC3** involves dearomatization of internally aromatic metallacycle, which is similar to the previously reported metal-ligand cooperation via dearomatization-aromatization process of ligand (Gunanathan and Milstein, 2011; Zeng et al., 2014; Khusnutdinova and Milstein, 2015; Li et al., 2019) The subsequent proton transfer from C1–H to the distal oxygen atom of Os–OOH (**TS3**) leads to the heterolytic cleavage of O–O bond and the formation of osmium-oxo species (Os=O) in **IC4**. Meanwhile, the internal aromaticity for metallacycle was recovered. This step experiences an overall Gibbs energy barrier of 24.2 kcal/mol (**TS3**) and constitutes the rate-determining step for the overall transformations. Such computational finding is in accordance with KIE experiments that the hydrogen originally from substrate C-H bond participates in the rate-determining transformations.

To complete the catalytic cycle, we proceed to consider the Os=O-mediated oxidation of alcohols. The calculated free energy profile is depicted in Figure 6. It is seen that the formation of aldehyde occurs via a double-hydrogen shift mechanism (**TS4**), in which the proton from the hydroxyl group shifts to oxo of Os=O species, whereas the hydride from the benzylic CH_2 group shifts to the metal center. Such mechanism is analogous to the osmium-peroxo-catalyzed oxidation of alcohol via **TS1**. This step experiences a Gibbs energy barrier of 16.5 kcal/mol relative to **IC5**, leading to the formation of aldehyde product and osmium-hydrido-hydroxo species (OsH(OH)) in **IC6**. All these indicate that the reactivity of osmium-oxo is much higher than that of osmium-peroxo species. The final hydride shift to the neighboring C1, followed by the H_2O formation, recovers the initial state of osmium-peroxo species **RC0** (Figure S12, and see also

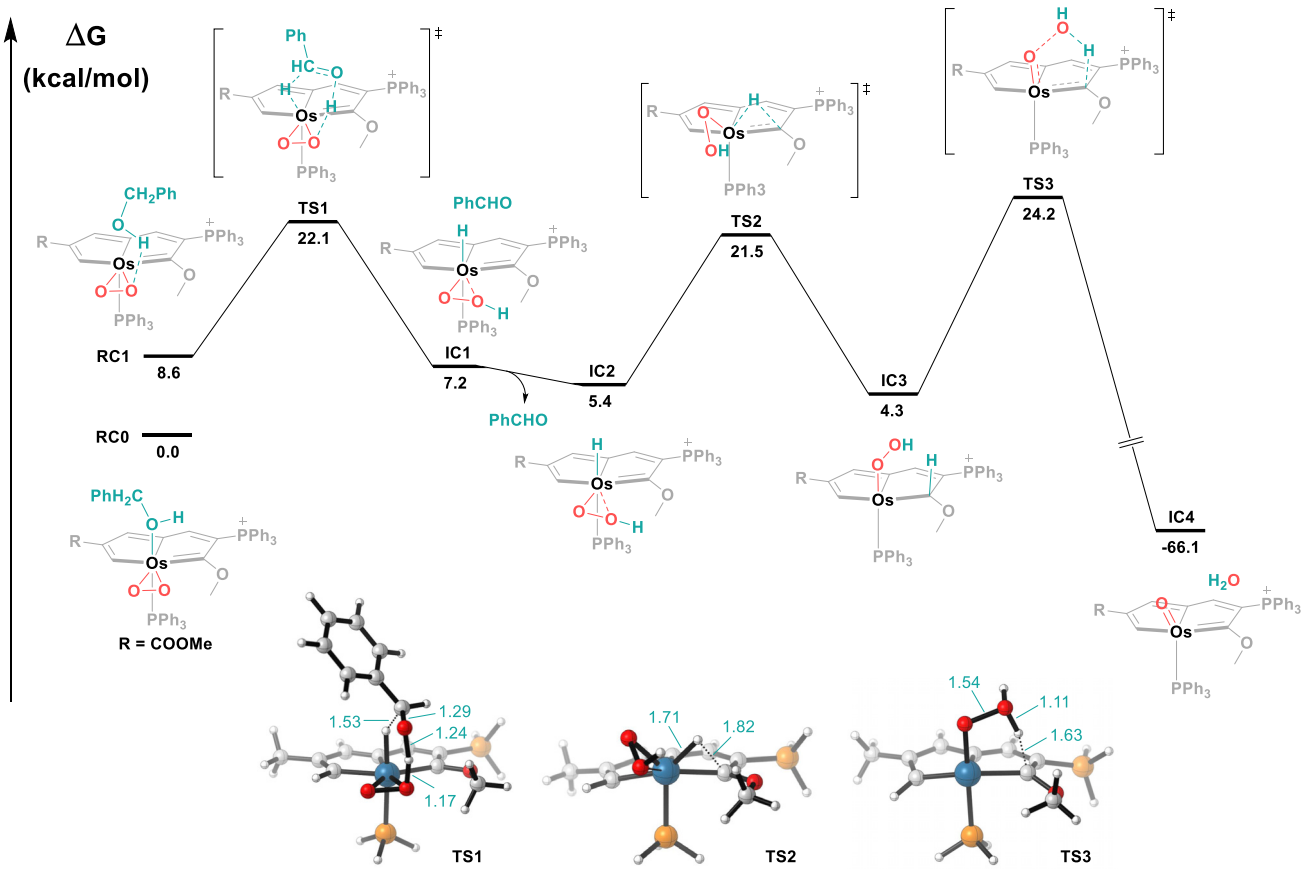

Figure 5. DFT-Computed Gibbs Energy Profile (in kcal/mol) for the Osmium-Peroxo-Catalyzed Aerobic Oxidation of Alcohol

Key distances are given in angstroms.

See also Figures S7–S11 and S13.

Figure S13 for full catalytic mechanism). Our calculations demonstrate that hydrogen transfer in **TS3**, where the hydrogen is initially derived from the benzylic CH_2 group of alcohol, is involved in the rate-determining step in overall transformations. This is in line with our experimental findings. As such, our computational studies reveal that both osmium-peroxo and oxo species act as the reactive intermediate toward alcohol oxidations. Interestingly, the internally aromatic metallacycle plays an unusual role in catalysis by facile metal-ligand cooperative catalysis through reversible dearomatization-aromatization. Such reversible transformation would facilitate the Os–OOH→Os=O conversion via the neighboring carbon site-assisted proton transfer, and thus significantly enhance the catalytic reactivity of **2**. This also explains why the osmium-peroxo species **2** could serve as an oxidant in the promoterless alcohol oxidations, whereas most of the previously catalytic processes require additives, such as nitroxyl radicals and base, to complete the catalytic cycle (Kopylovich et al., 2015).

Conclusion

In this work, we demonstrated that the relatively stable osmium-peroxo species can be achieved through the reaction of osmapentalyne with molecular oxygen in the presence of nucleophile. The peroxo ligand was almost symmetrically bound to the metal center in a side-on fashion determined from X-ray crystal structure. DFT calculations together with experiments showed that the aromaticity of metallacycle provided the stability for active osmium-peroxo species, which was also capable of promoterless alcohol dehydrogenation. Different from the commonly proposed β-hydride elimination mechanisms for alcohol oxidation, our calculations demonstrate that the osmium-peroxo-catalyzed aerobic oxidation of alcohol proceeds via the concerted double-hydrogen transfer mechanism, affording the osmium-hydrido-hydroperoxo species (OsH(OOH)) and aldehyde in one step. The subsequent ligand-assisted O–O

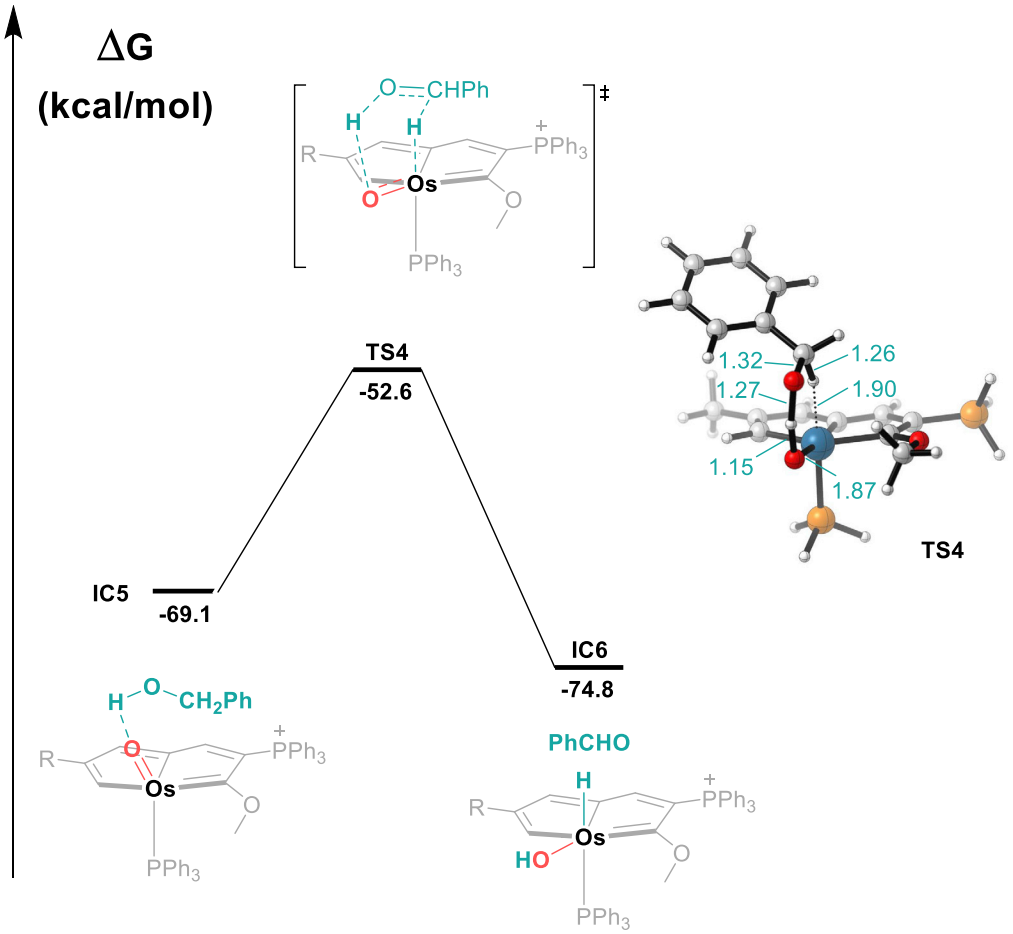

Figure 6. DFT-Computed Reaction Gibbs Energy Profile (in kcal/mol) for the Osmium-Oxo-Catalyzed Aerobic Oxidation of Alcohol

Key distances are given in angstroms.

See also Figures S12 and S13.

heterolytic cleavage in OsH(OOH) generates the second active species of osmium-oxo complex (Os=O) for alcohol oxidation. Thus the catalysis involves an unusual dearomatization-aromatization of metallacycle. The kinetic results and theoretical calculations suggest that the turnover-limiting step involves the transfer of a hydrogen atom derived from the benzylic CH_2 of the substrate. These observations represent the rare examples of structurally characterized metal-peroxo complex in the aerobic oxidation of alcohol, and mechanistic insights could help to develop the new and more efficient catalytic systems for green and sustainable chemistry. Moreover, it is expected that the osmium-peroxo complex synthesized here could be applied to the promoterless oxidations of other substrates, such as amines.

Limitations of the Study

Alkene oxidation was also studied under the present catalytic conditions, but no hydroxylation or epoxidation products were observed.

Resource Availability

Lead Contact

Further information and requests for resources should be directed to and will be fulfilled by the Lead Contact, Haiping Xia (hpxia@xmu.edu.cn).

Materials Availability

Any materials generated in this study are available from the Lead Contact without restriction.

Data and Code Availability

The accession number for the crystallographic data of complex **2** reported in this paper is Cambridge Crystallographic Data Center: 1892835.

METHODS

All methods can be found in the accompanying Transparent Methods supplemental file.

SUPPLEMENTAL INFORMATION

Supplemental Information can be found online at https://doi.org/10.1016/j.isci.2020.101379.

ACKNOWLEDGMENTS

We gratefully thank the financial supports from the National Natural Science Foundation of China (21931002, 21871225, and 21907082).

AUTHOR CONTRIBUTIONS

H.X. and B.W. conceived the study. Z.D. and Y.S. carried out experimental work, P.W. and Y.C. carried out computational studies, and Z.C. solved the X-ray structure. H.X., B.W., H.Z., and Z.D. analyzed the data and wrote the manuscript.

DECLARATION OF INTERESTS

The authors declare no competing interests.

Received: May 8, 2020
Revised: June 14, 2020
Accepted: July 14, 2020
Published: August 21, 2020

REFERENCES

Arends, I.W.C.E., and Sheldon, R.A. (2004). Modern oxidation of alcohols using environmentally benign oxidants. In Modern Oxidation Methods, J.E. Bäckvall, ed. (Wiley-VCH), pp. 83–118.

Baglia, R.A., Zaragoza, J.P.T., and Goldberg, D.P. (2017). Biomimetic reactivity of oxygen-derived manganese and iron porphyrinoid complexes. Chem. Rev. *117*, 13320–13352.

Barman, P., Cantú Reinhard, F.G., Bagha, U.K., Kumar, D., Sastri, C.V., and de Visser, S.P. (2019). Hydrogen by deuterium substitution in an aldehyde tunes the regioselectivity by a nonheme manganese(III)–peroxo complex. Angew. Chem. Int. Ed. *58*, 10639–10643.

Bianchini, C., Meli, A., Peruzzini, M., and Vizza, F. (1990). Oxidation of primary alcohols to carboxylic acids made easy at iridium. J. Am. Chem. Soc. *112*, 6726–6728.

Brink, G.t., Arends, I.W.C.E., and Sheldon, R.A. (2000). Green, catalytic oxidation of alcohols in water. Science *287*, 1636–1639.

Chen, J.X., and Jia, G.C. (2013). Recent development in the chemistry of transition metal-containing metallabenzenes and metallabenzynes. Coord. Chem. Rev. *257*, 2491–2521.

Chen, Z.W., Wannere, C.S., Corminboeuf, C., Puchta, R., and Schleyer, P.v.R. (2005). Nucleus-independent chemical shifts (NICS) as an aromaticity criterion. Chem. Rev. *105*, 3842–3888.

Cho, J., Jeon, S., Wilson, S.A., Liu, L.V., Kang, E.A., Braymer, J.J., Lim, M.H., Hedman, B., Hodgson, K.O., Valentine, J.S., et al. (2011). Structure and reactivity of a mononuclear non-haem iron(III)-peroxo complex. Nature *478*, 502–505.

Cho, K.-B., Hirao, H., Shaik, S., and Nam, W. (2016). To rebound or dissociate? This is the mechanistic question in C–H hydroxylation by heme and nonheme metal–oxo complexes. Chem. Soc. Rev. *45*, 1197–1210.

Chung, K., Banik, S.M., De Crisci, A.G., Pearson, D.M., Blake, T.R., Olsson, J.V., Ingram, A.J., Zare, R.N., and Waymouth, R.M. (2013). Chemoselective Pd-catalyzed oxidation of polyols: synthetic scope and mechanistic studies. J. Am. Chem. Soc. *135*, 7593–7602.

Cook, S.A., and Borovik, A.S. (2015). Molecular designs for controlling the local environments around metal ions. Acc. Chem. Res. *48*, 2407–2414.

Costas, M., Mehn, M.P., Jensen, M.P., and Que, L. (2004). Dioxygen activation at mononuclear nonheme iron active sites: enzymes, models, and intermediates. Chem. Rev. *104*, 939–986.

Dong, G., Shaik, S., and Lai, W. (2013). Oxygen activation by homoprotocatechuate 2,3-dioxygenase: a QM/MM study reveals the key intermediates in the activation cycle. Chem. Sci. *4*, 3624–3635.

Elwell, C.E., Gagnon, N.L., Neisen, B.D., Dhar, D., Spaeth, A.D., Yee, G.M., and Tolman, W.B. (2017). Copper–oxygen complexes revisited: structures, spectroscopy, and reactivity. Chem. Rev. *117*, 2059–2107.

Esteruelas, M.A., García-Obregón, T., Herrero, J., and Oliván, M. (2011). Osmium-catalyzed oxidation of primary alcohols with molecular oxygen. Organometallics *30*, 6402–6407.

Fallah-Bagher-Shaidaei, H., Wannere, C.S., Corminboeuf, C., Puchta, R., and Schleyer, P.v.R. (2006). Which NICS aromaticity index for planar π rings is best? Org. Lett. *8*, 863–866.

Fernández, I., Frenking, G., and Merino, G. (2015). Aromaticity of metallabenzenes and related compounds. Chem. Soc. Rev. *44*, 6452–6463.

Frogley, B.J., and Wright, L.J. (2018). Recent advances in metallaaromatic chemistry. Chem. Eur. J. *24*, 2025–2038.

Geuenich, D., Hess, K., Köhler, F., and Herges, R. (2005). Anisotropy of the induced current density (ACID), a general method to quantify and visualize electronic delocalization. Chem. Rev. *105*, 3758–3772.

Gordon, J.B., Vilbert, A.C., Siegler, M.A., Lancaster, K.M., Moenne-Loccoz, P., and Goldberg, D.P. (2019). A nonheme thiolate-ligated cobalt superoxo complex: synthesis and spectroscopic characterization, computational studies, and hydrogen atom abstraction reactivity. J. Am. Chem. Soc. *141*, 3641–3653.

Gunanathan, C., and Milstein, D. (2011). Metal–ligand cooperation by aromatization–dearomatization: a new paradigm in bond activation and "green" catalysis. Acc. Chem. Res. *44*, 588–602.

Herges, R., and Geuenich, D. (2001). Delocalization of electrons in molecules. J. Phys. Chem. A *105*, 3214–3220.

Hong, S., Lee, Y.-M., Ray, K., and Nam, W. (2017). Dioxygen activation chemistry by synthetic mononuclear nonheme iron, copper and chromium complexes. Coord. Chem. Rev. *334*, 25–42.

Hu, X., Castro-Rodriguez, I., and Meyer, K. (2004). Dioxygen activation by a low-valent cobalt complex employing a flexible tripodal N-heterocyclic carbene ligand. J. Am. Chem. Soc. *126*, 13464–13473.

Jones, W.D. (2003). Isotope effects in C−H bond activation reactions by transition metals. Acc. Chem. Res. *36*, 140–146.

Karlin, K.D. (2010). Model offers intermediate insight. Nature *463*, 168–169.

Karlsson, A.P., Parales, J.V., Parales, R.E., Gibson, D.T., Eklund, H., and Ramaswamy, S. (2003). Crystal structure of naphthalene dioxygenase: side-on binding of dioxygen to iron. Science *299*, 1039–1042.

Khusnutdinova, J.R., and Milstein, D. (2015). Metal–ligand cooperation. Angew. Chem. Int. Ed. *54*, 12236–12273.

Konnick, M.M., and Stahl, S.S. (2008). Reaction of molecular oxygen with a PdII-hydride to produce a PdII-hydroperoxide: experimental evidence for an HX-reductive-elimination pathway. J. Am. Chem. Soc. *130*, 5753–5762.

Kopylovich, M.N., Ribeiro, A.P.C., Alegria, E.C.B.A., Martins, N.M.R., Martins, L.M.D.R.S., and Pombeiro, A.J.L. (2015). Chapter three - catalytic oxidation of alcohols: recent advances. In Advances in Organometallic Chemistry, P.J. Pérez, ed. (Academic Press), pp. 91–174.

Kovacs, J.A. (2015). Tuning the relative stability and reactivity of manganese dioxygen and peroxo intermediates via systematic ligand modification. Acc. Chem. Res. *48*, 2744–2753.

Krygowski, T.M., and Cyrański, M.K. (2001). Structural aspects of aromaticity. Chem. Rev. *101*, 1385–1420.

Landorf, C.W., and Haley, M.M. (2006). Recent advances in metallabenzene chemistry. Angew. Chem. Int. Ed. *45*, 3914–3936.

Lee, C.-M., Chuo, C.-H., Chen, C.-H., Hu, C.-C., Chiang, M.-H., Tseng, Y.-J., Hu, C.-H., and Lee, G.-H. (2012). Structural and spectroscopic characterization of a monomeric side-on manganese(IV) peroxo complex. Angew. Chem. Int. Ed. *51*, 5427–5430.

Lewis, E.A., and Tolman, W.B. (2004). Reactivity of dioxygen−copper systems. Chem. Rev. *104*, 1047–1076.

Li, H., Gonçalves, T.P., Lupp, D., and Huang, K.-W. (2019). PN3(P)-pincer complexes: cooperative catalysis and beyond. ACS Catal. *9*, 1619–1629.

Maddock, S.M., Rickard, C.E.F., Roper, W.R., and Wright, L.J. (1996). Seven-coordinate dioxygen complexes from dioxygen addition to five-coordinate σ-phenyl, isocyanide-containing derivatives of ruthenium(II) and osmium(II). Crystal structures of OS(η2-O2)(η2-CPh = Np-chlorophenyl)Cl(PPh3)2 and Os(η2-SO4)(η2-CPh = Np-chlorophenyl)Cl(PPh3)2. J. Organomet. Chem. *510*, 267–279.

Meunier, B. (2000). Metal-Oxo and Metal-Peroxo Species in Catalytic Oxidations (Springer Berlin Heidelberg).

Mezzetti, A., Zangrando, E., Del Zotto, A., and Rigo, P. (1994). Dioxygen addition to five-coordinate osmium(II) complexes. X-Ray crystal structure of [OsH(η2–O2)(dcpe)2]bph4[dcpe = 1,2-bis(dicyclohexylphosphino)ethane]. J. Chem. Soc. Chem. Commun. *13*, 1597–1598.

Mirica, L.M., Ottenwaelder, X., and Stack, T.D.P. (2004). Structure and spectroscopy of copper−dioxygen complexes. Chem. Rev. *104*, 1013–1046.

Nam, W. (2015). Synthetic mononuclear nonheme iron–oxygen intermediates. Acc. Chem. Res. *48*, 2415–2423.

Neu, H.M., Baglia, R.A., and Goldberg, D.P. (2015). A balancing act: stability versus reactivity of Mn(O) complexes. Acc. Chem. Res. *48*, 2754–2764.

Ohta, T., Liu, J.-G., and Naruta, Y. (2013). Resonance Raman characterization of mononuclear heme-peroxo intermediate models. Coord. Chem. Rev. *257*, 407–413.

Parmeggiani, C., and Cardona, F. (2012). Transition metal based catalysts in the aerobic oxidation of alcohols. Green. Chem. *14*, 547–564.

Punniyamurthy, T., Velusamy, S., and Iqbal, J. (2005). Recent advances in transition metal catalyzed oxidation of organic substrates with molecular oxygen. Chem. Rev. *105*, 2329–2364.

Quist, D.A., Diaz, D.E., Liu, J.J., and Karlin, K.D. (2017). Activation of dioxygen by copper metalloproteins and insights from model complexes. J. Biol. Inorg. Chem. *22*, 253–288.

Rajabimoghadam, K., Darwish, Y., Bashir, U., Pitman, D., Eichelberger, S., Siegler, M.A., Swart, M., and Garcia-Bosch, I. (2018). Catalytic aerobic oxidation of alcohols by copper complexes bearing redox-active ligands with tunable H-bonding groups. J. Am. Chem. Soc. *140*, 16625–16634.

Ryland, B.L., and Stahl, S.S. (2014). Practical aerobic oxidations of alcohols and amines with homogeneous copper/TEMPO and related catalyst systems. Angew. Chem. Int. Ed. *53*, 8824–8838.

Sacramento, J.J.D., and Goldberg, D.P. (2018). Factors affecting hydrogen atom transfer reactivity of metal-oxo porphyrinoid complexes. Acc. Chem. Res. *51*, 2641–2652.

Schleyer, P.v.R. (2001). Introduction: aromaticity. Chem. Rev. *101*, 1115–1118.

Schleyer, P.v.R., and Pühlhofer, F. (2002). Recommendations for the evaluation of aromatic stabilization energies. Org. Lett. *4*, 2873–2876.

Schleyer, P.v.R., Maerker, C., Dransfeld, A., Jiao, H., and van Eikema Hommes, N.J.R. (1996). Nucleus-independent chemical shifts: a simple and efficient aromaticity probe. J. Am. Chem. Soc. *118*, 6317–6318.

Shi, Z., Zhang, C., Tang, C., and Jiao, N. (2012). Recent advances in transition-metal catalyzed reactions using molecular oxygen as the oxidant. Chem. Soc. Rev. *41*, 3381–3430.

Shook, R.L., Gunderson, W.A., Greaves, J., Ziller, J.W., Hendrich, M.P., and Borovik, A.S. (2008). A monomeric MnIII−peroxo complex derived directly from dioxygen. J. Am. Chem. Soc. *130*, 8888–8889.

Sigman, M.S., and Jensen, D.R. (2006). Ligand-modulated palladium-catalyzed aerobic alcohol oxidations. Acc. Chem. Res. *39*, 221–229.

Simmons, E.M., and Hartwig, J.F. (2012). On the interpretation of deuterium kinetic isotope effects in C-H bond functionalizations by transition-metal complexes. Angew. Chem. Int. Ed. *51*, 3066–3072.

Solomon, E.I., Heppner, D.E., Johnston, E.M., Ginsbach, J.W., Cirera, J., Qayyum, M., Kieber-Emmons, M.T., Kjaergaard, C.H., Hadt, R.G., and Tian, L. (2014). Copper active sites in biology. Chem. Rev. *114*, 3659–3853.

Stahl, S.S. (2004). Palladium oxidase catalysis: selective oxidation of organic chemicals by direct dioxygen-coupled turnover. Angew. Chem. Int. Ed. *43*, 3400–3420.

Stahl, S.S. (2005). Palladium-catalyzed oxidation of organic chemicals with O2. Science *309*, 1824–1826.

Tojo, G., and Marcos, I.F. (2006). Oxidation of Alcohols to Aldehydes and Ketones (Springer).

Tronic, T.A., Rakowski DuBois, M., Kaminsky, W., Coggins, M.K., Liu, T., and Mayer, J.M. (2011). Directing protons to the dioxygen ligand of a ruthenium(II) complex with pendent amines in the second coordination sphere. Angew. Chem. Int. Ed. *50*, 10936–10939.

Waidmann, C.R., DiPasquale, A.G., and Mayer, J.M. (2010). Synthesis and reactivity of oxo-peroxo-vanadium(V) bipyridine compounds. Inorg. Chem. *49*, 2383–2391.

Wannere, C.S., Moran, D., Allinger, N.L., Hess, B.A., Schaad, L.J., and Schleyer, P.v.R. (2003). On the stability of large [4n]annulenes. Org. Lett. *5*, 2983–2986.

Wei, J., Zhang, W.X., and Xi, Z. (2018). The aromatic dianion metalloles. Chem. Sci. *9*, 560–568.

Yan Poon, P.C., Dedushko, M.A., Sun, X., Yang, G., Toledo, S., Hayes, E.C., Johansen, A., Piquette, M.C., Rees, J.A., Stoll, S., et al. (2019). How metal ion lewis acidity and steric properties influence the barrier to dioxygen binding, peroxo O–O bond cleavage, and reactivity. J. Am. Chem. Soc. *141*, 15046–15057.

Yee, G.M., and Tolman, W.B. (2015). Transition metal complexes and the activation of dioxygen. In Sustaining Life on Planet Earth: Metalloenzymes Mastering Dioxygen and Other Chewy Gases, P.M.H. Kroneck and M.E. Sosa Torres, eds. (Springer International Publishing), pp. 131–204.

Zeng, G., Sakaki, S., Fujita, K.-i., Sano, H., and Yamaguchi, R. (2014). Efficient catalyst for acceptorless alcohol dehydrogenation: interplay of theoretical and experimental studies. ACS Catal. *4*, 1010–1020.

Zhu, C., and Xia, H. (2018). Carbolong chemistry: a story of carbon chain ligands and transition metals. Acc. Chem. Res. *51*, 1691–1700.

Zhu, C., Li, S., Luo, M., Zhou, X., Niu, Y., Lin, M., Zhu, J., Cao, Z., Lu, X., Wen, T., et al. (2013). Stabilization of anti-aromatic and strained five-membered rings with a transition metal. Nat. Chem. *5*, 698–703.

Zhu, C., Yang, Y., Luo, M., Yang, C., Wu, J., Chen, L., Liu, G., Wen, T., Zhu, J., and Xia, H. (2015). Stabilizing two classical antiaromatic frameworks: demonstration of photoacoustic imaging and the photothermal effect in metalla-aromatics. Angew. Chem. Int. Ed. *54*, 6181–6185.

Zhuo, Q., Zhang, H., Ding, L., Lin, J., Zhou, X., Hua, Y., Zhu, J., and Xia, H. (2019). Rhodapentalenes: pincer complexes with internal aromaticity. iScience *19*, 1214–1224.

iScience, Volume *23*

Supplemental Information

Dioxygen Activation by Internally Aromatic Metallacycle: Crystallographic Structure and Mechanistic Investigations

Zhihong Deng, Peng Wu, Yapeng Cai, Yanheng Sui, Zhixin Chen, Hong Zhang, Binju Wang, and Haiping Xia

The Supplementary Materials include:

Supplemental Figures

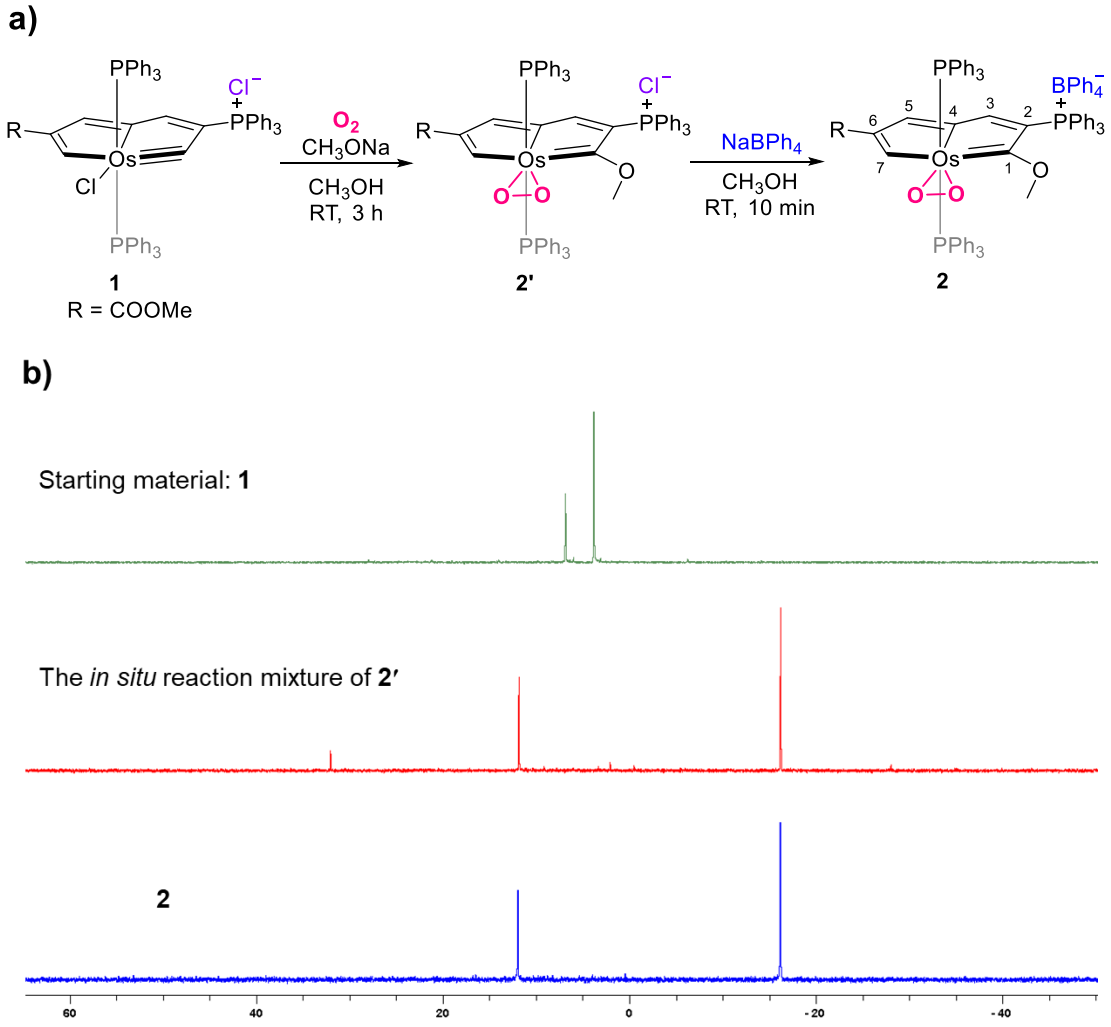

Figure S1. (a) Synthesis of osmium-peroxo complexes. **(b)** In situ NMR monitoring for the generation of **2**. Overlapping $^{31}P\{^{1}H\}$ NMR spectrums of **1**, the *in situ* reaction mixture of **2′** (**1**+CH_3ONa+O_2, CH_3OH, RT, 3 h), and **2**. The similar nuclear magnetic resonance (NMR) spectrums of **2′** and **2** suggest the same cation of them. Related to Scheme 1.

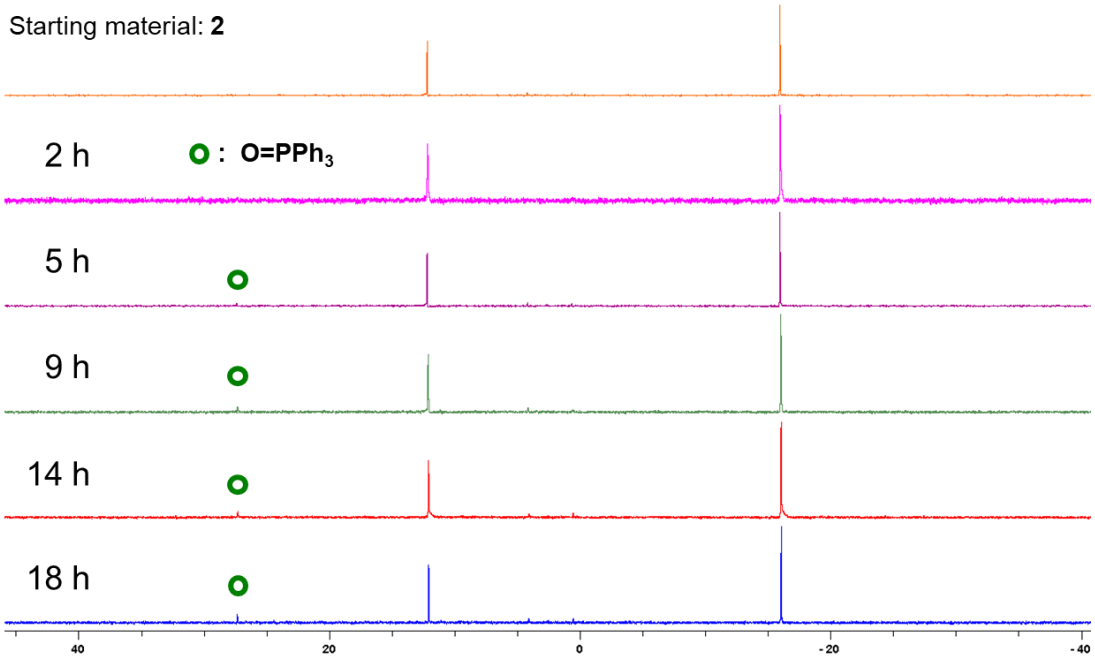

Figure S2. Thermal stability tests of **2** observed by $^{31}P\{^{1}H\}$ NMR. Test conditions: 1,2-dichloroethane, air, 60 °C. Related to Scheme 1.

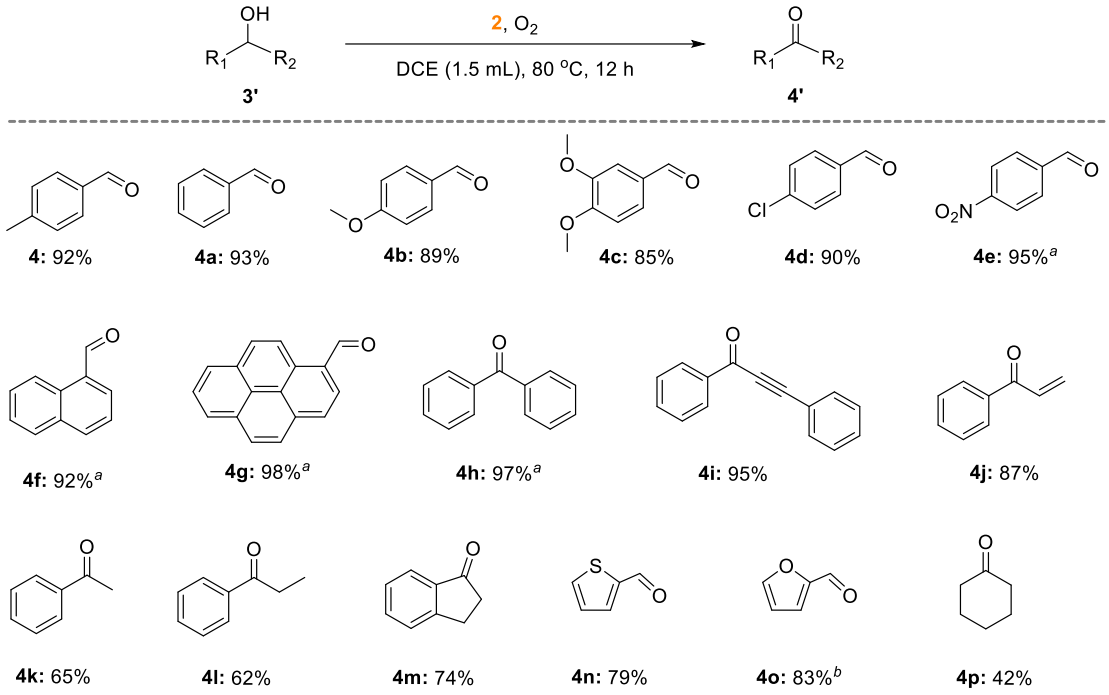

Figure S3. Substrate scope for the aerobic catalytic oxidation of various alcohols. Reaction conditions: alcohol (0.3 mmol), catalyst (**2**, 5 mol%), DCE (1,2-dichloroethane,1.5 mL), under 1.5 atm of O_2, and 12 hours reaction time at 80 °C. Isolated yield. [a]Catalyst loading (3 mol%). [b]Yield was determined by GC using mesitylene as an internal standard due to the product volatility. Related to Figure 4.

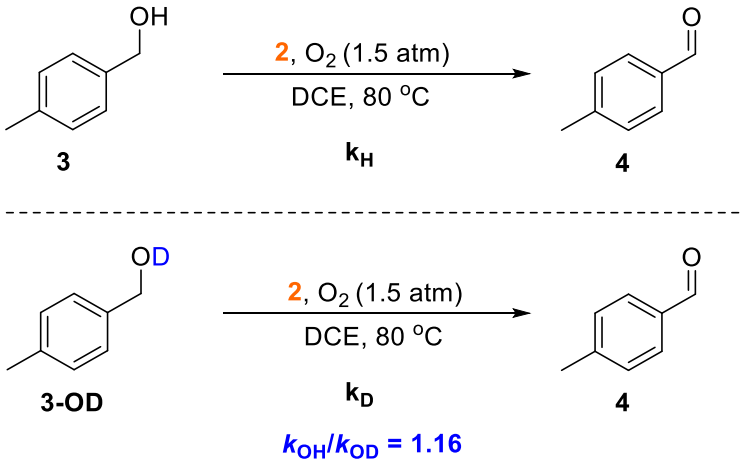

Figure S4. KIE on k_{OH}/k_{OD} was determined from two parallel reactions using **3** (109.8 mg, 0.9 mmol) and **3-OD** (110.7 mg, 0.9 mmol; approximately 97% D-enriched) as substrates respectively. The procedure was similar to that described in Figure S5. Related to Figure 4.

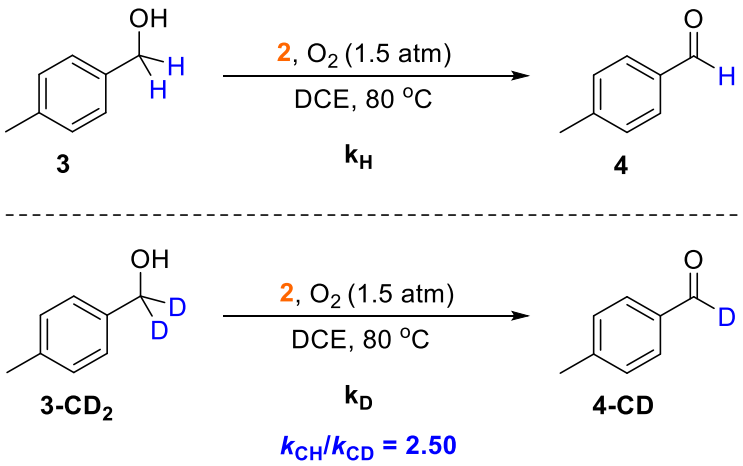

Figure S5. KIE on k_{CH}/k_{CD} was determined from two parallel reactions. Experimental procedure: **3** (109.8 mg, 0.9 mmol) and **3-CD$_2$** (111.6 mg, 0.9 mmol; approximately 95% D-enriched) were placed in a dried reaction tube with an inner volume of 50 mL respectively, and then treated with the same mixture of 2 (5% mmol), mesitylene (internal standard, 60 μL) in freshly distilled DCE (4.5 mL) at 80 ˚C under O_2 atmosphere (1.5 atm). Each reaction was stopped after desired time (every 20 minutes), the catalyst was separated by precipitation with ether, to extract 1 μL solution for GC analysis. The GC yields were calculated after calibrating the response of GC, and reactions with the two substrates were carried out in parallel to minimize experimental error. Related to Figure 4.

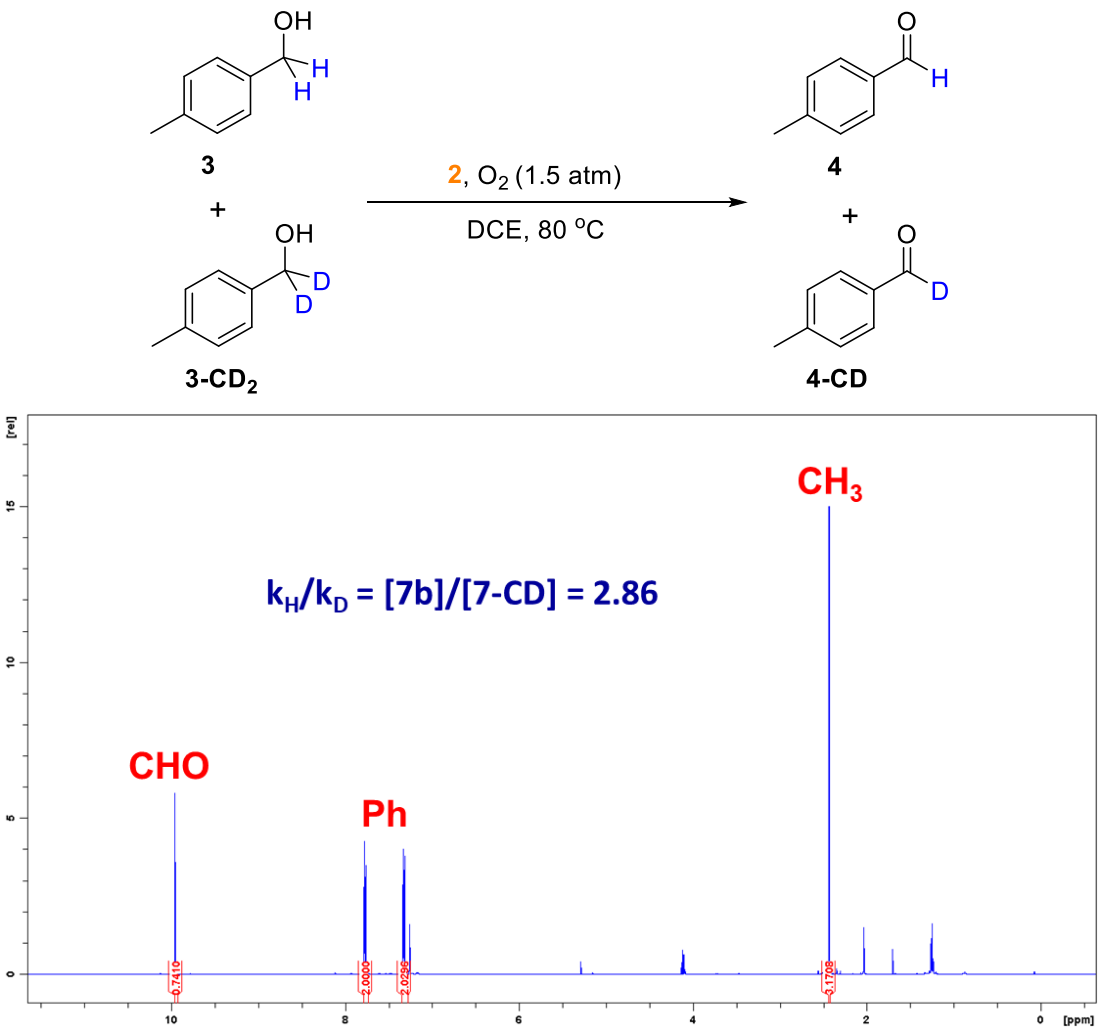

Figure S6. Intermolecular competition KIE experiments. KIE value was observed by ^{1}H NMR when the reaction was in low conversion. Reaction conditions: **3** (0.3 mmol), **3-CD2** (0.3 mmol), **2** (0.015 mmol), DCE (1,2-dichloroethane, 1.5 mL), under 1.5 atm of O_2, and 1 hour reaction time at 80 ˚C. After cooled to RT, the reaction mixture was isolated by flash silicon column chromatography to afford crude products containing **4** and **4-CD**. Related to Figure 4.

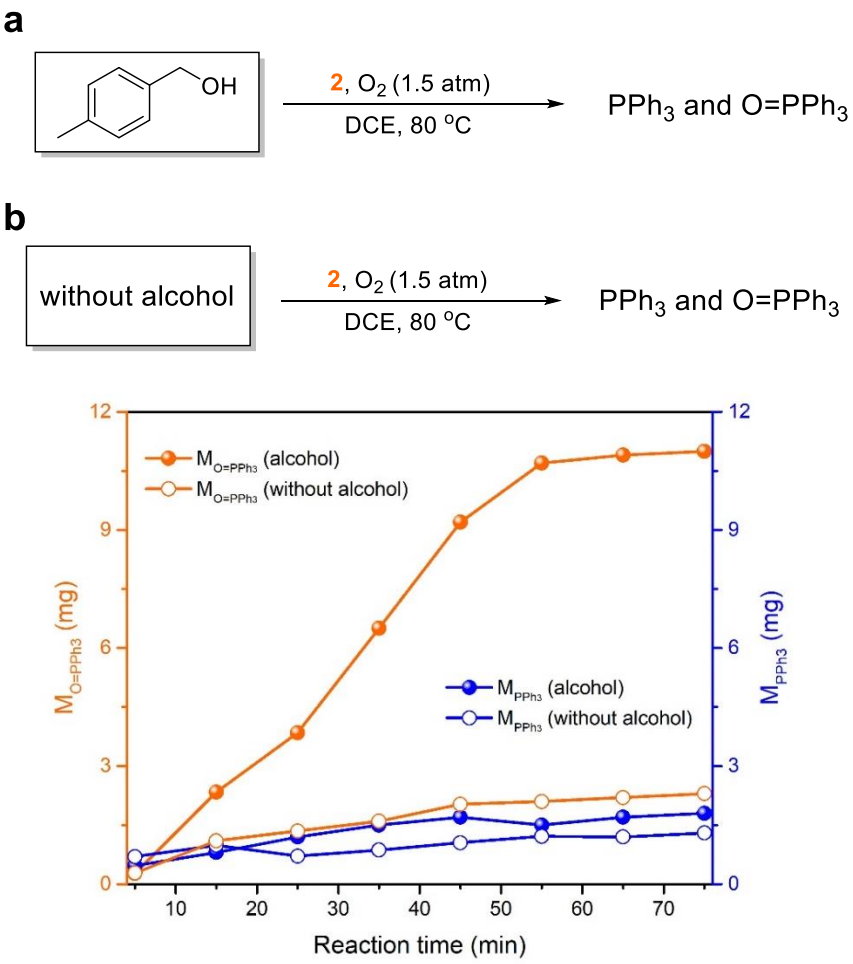

Figure S7. Detection of PPh_3 and $O{=}PPh_3$ in the initial stage of the reaction mixture with and without alcohol using GC-MS. (a) *p*-methylbenzyl alcohol (0.9 mmol), **2** (0.045 mmol, 5% mmol), DCE (1,2-dichloroethane, 4.5 mL), under 1.5 atm of O_2, and at 80 ˚C. (b) **2** (0.045 mmol), DCE (1,2-dichloroethane, 4.5 mL), under 1.5 atm of O_2, at 80 ˚C. The catalyst was separated by precipitation with ether, to extract 1 μL solution for GC-MS analysis. Related to Figure 5.

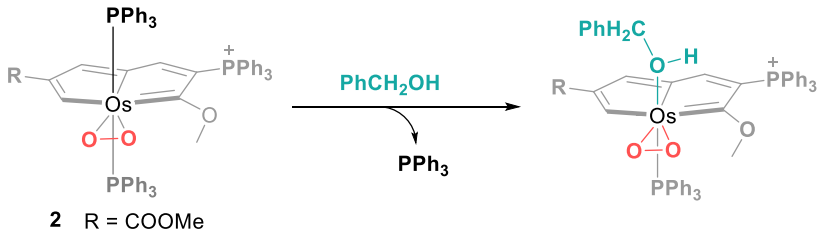

Figure S8. Dissociation of PPh_3 ligand from 2 and following alcohol coordination to the metal center. Related to Figure 5.

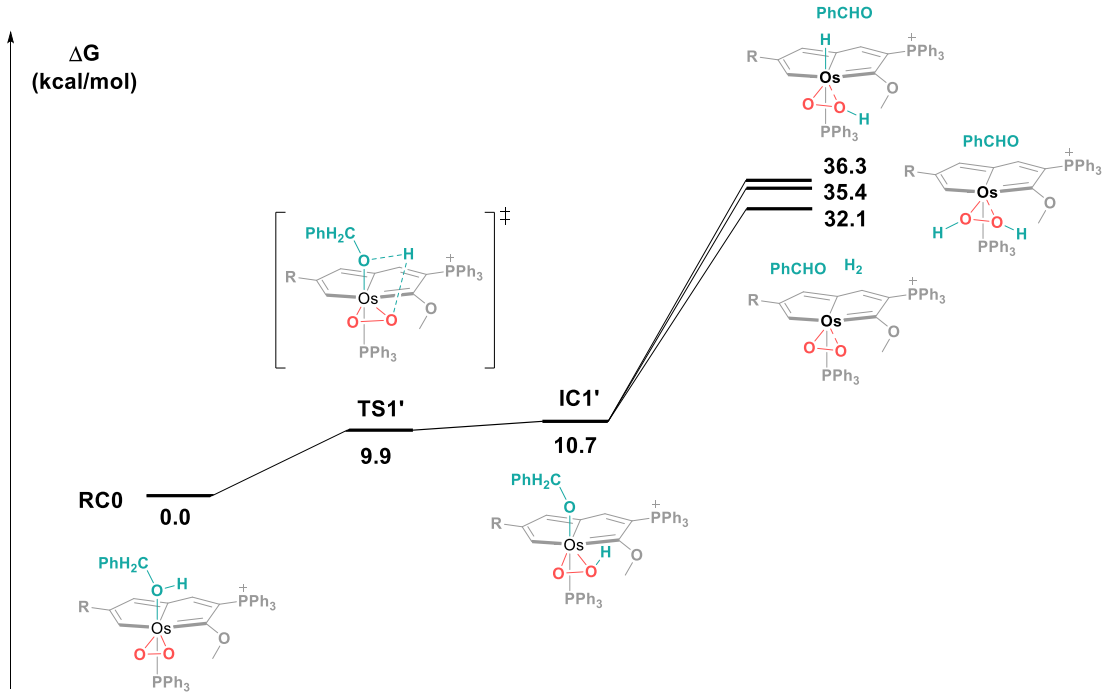

Figure S9. Calculated Gibbs energy profile (in kcal/mol) for the osmium-peroxo mediated aerobic oxidation of alcohol from **RC0**. The reaction is initiated with proton transfer from the hydroxyl group of substrate to peroxo moiety, followed by another hydride transfer in three possible pathways. Related to Figure 5.

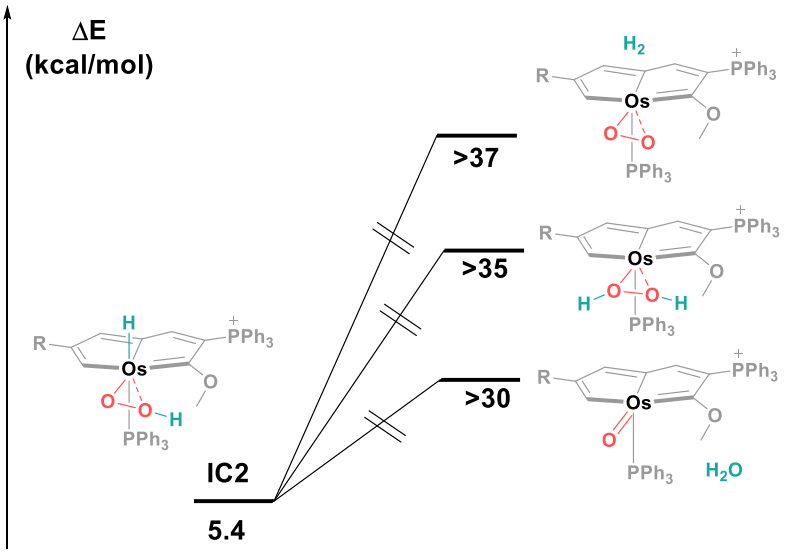

Figure S10. The scanned barriers (in kcal/mol) for the other three unfavorable reaction pathways from the OsH(OOH) intermediate **IC2**, including Os=O formation, H_2O_2 formation, as well as the H_2 formation. Related to Figure 5.

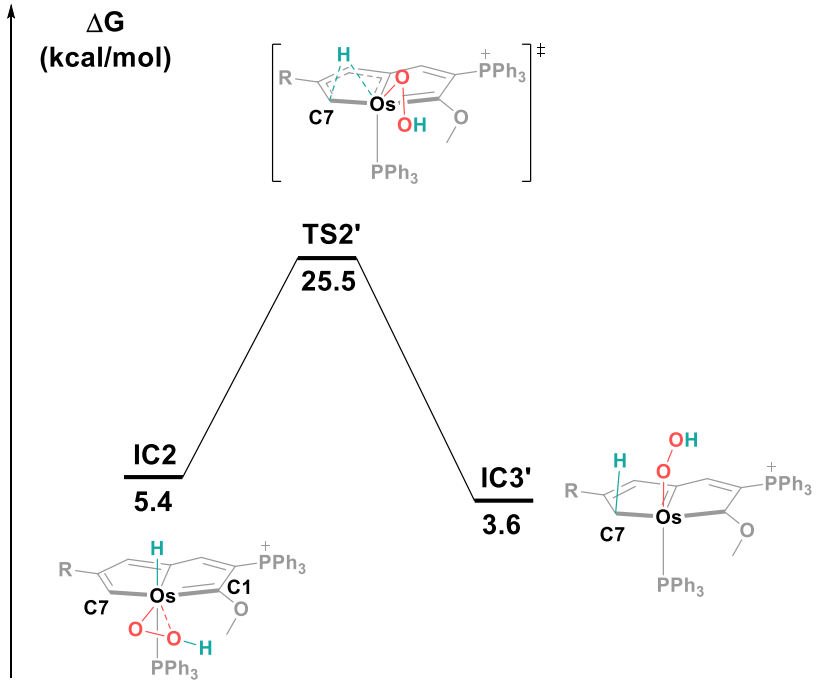

Figure S11. Calculated Gibbs energy barrier for the hydride transfer to the neighboring C7 from IC2. Related to Figure 5.

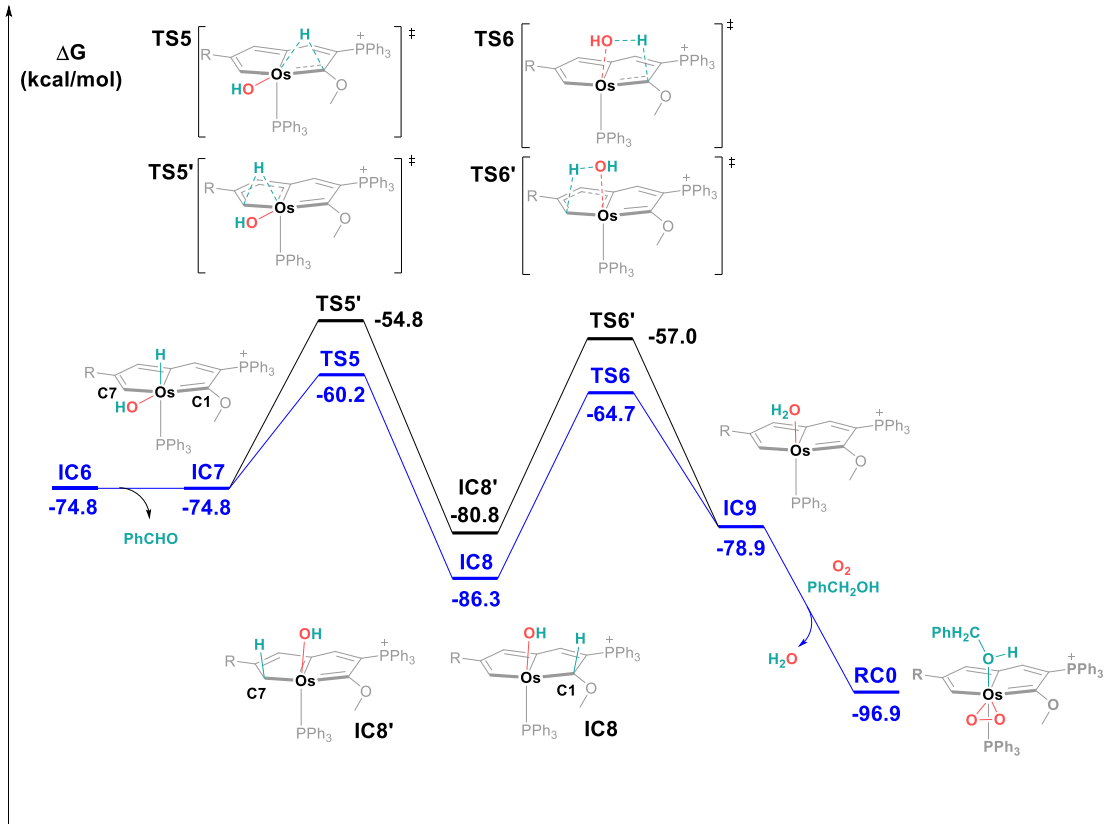

Figure S12. Calculated Gibbs energy profile for hydride transfer in IC7. The final hydride shift to the neighboring carbon (either C1 or C7), followed by the H_2O formation, O_2 coordination, and substrate binding. Related to Figure 6.

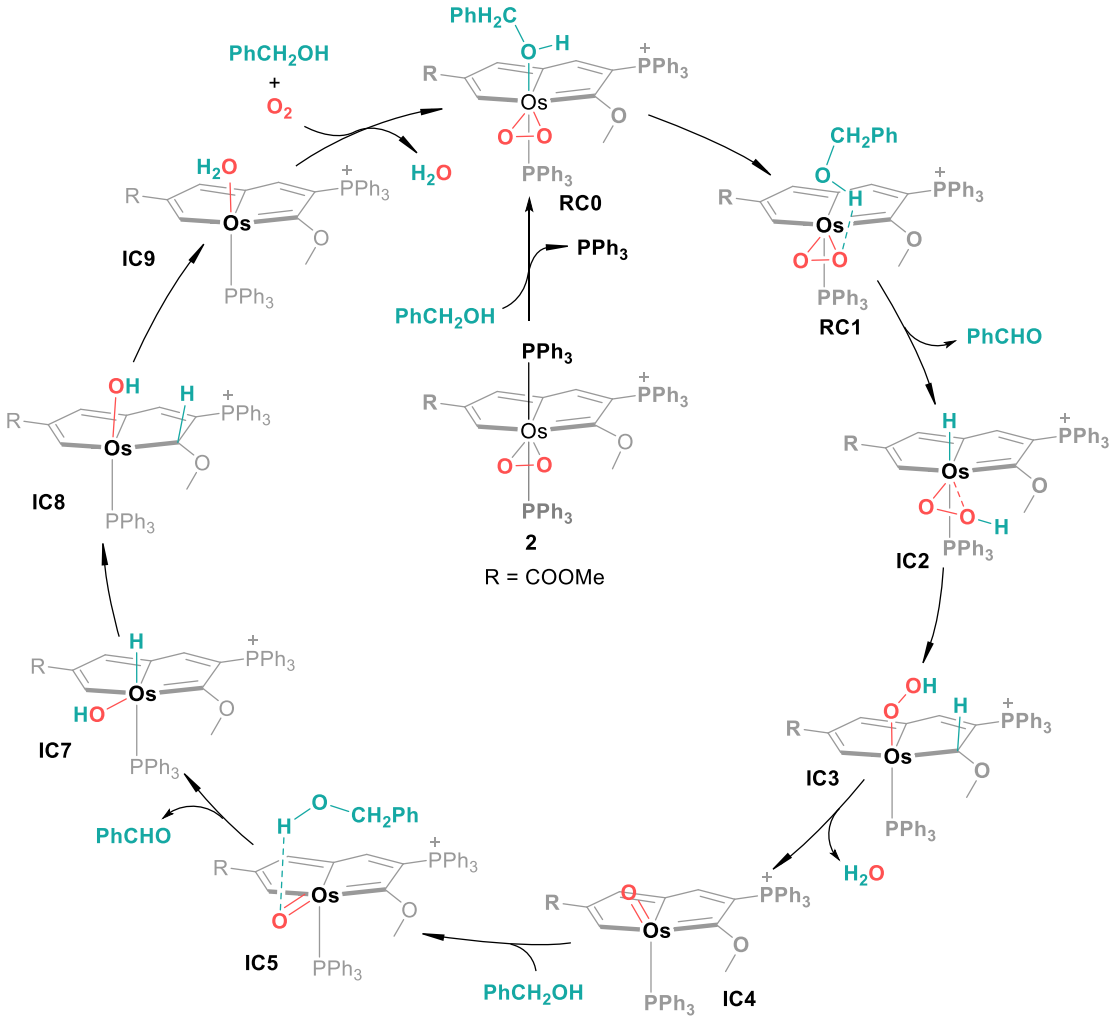

Figure S13. Full catalytic mechanism for the osmium-peroxo catalyzed aerobic oxidation of alcohol. Related to Figures 5 and 6.

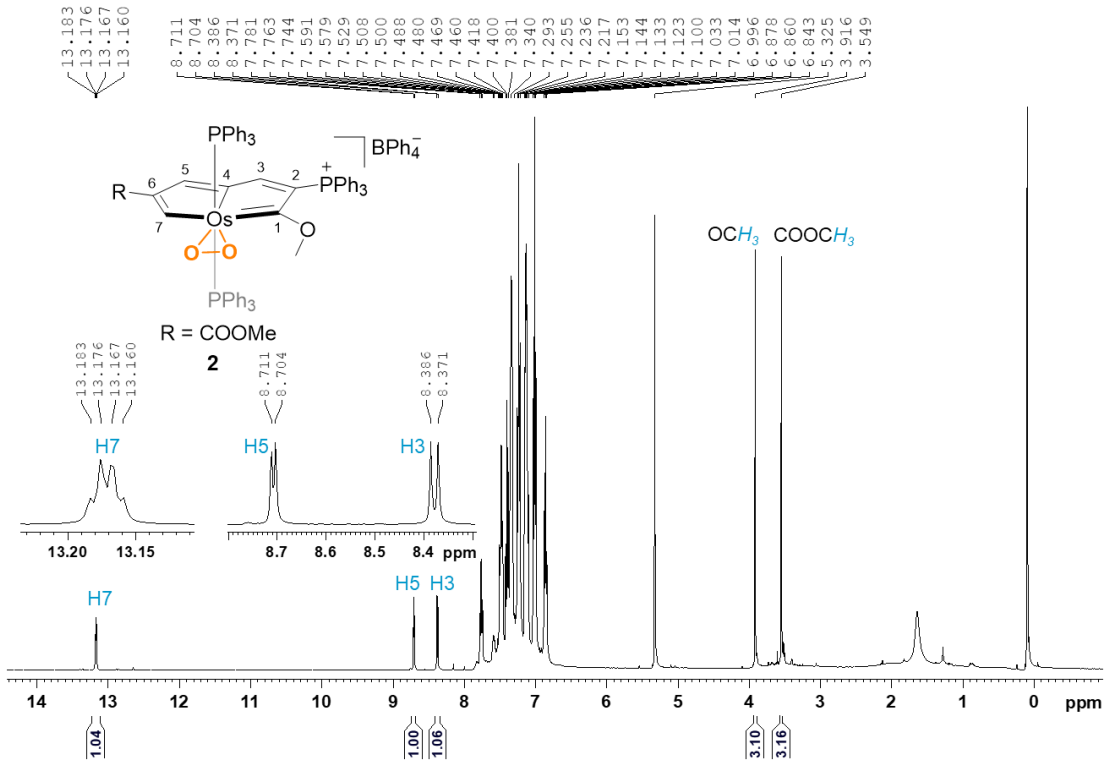

Figure S14. The ^{1}H NMR (400.1 MHz, CD_2Cl_2) spectrum for complex **2**. Related to Scheme 1.

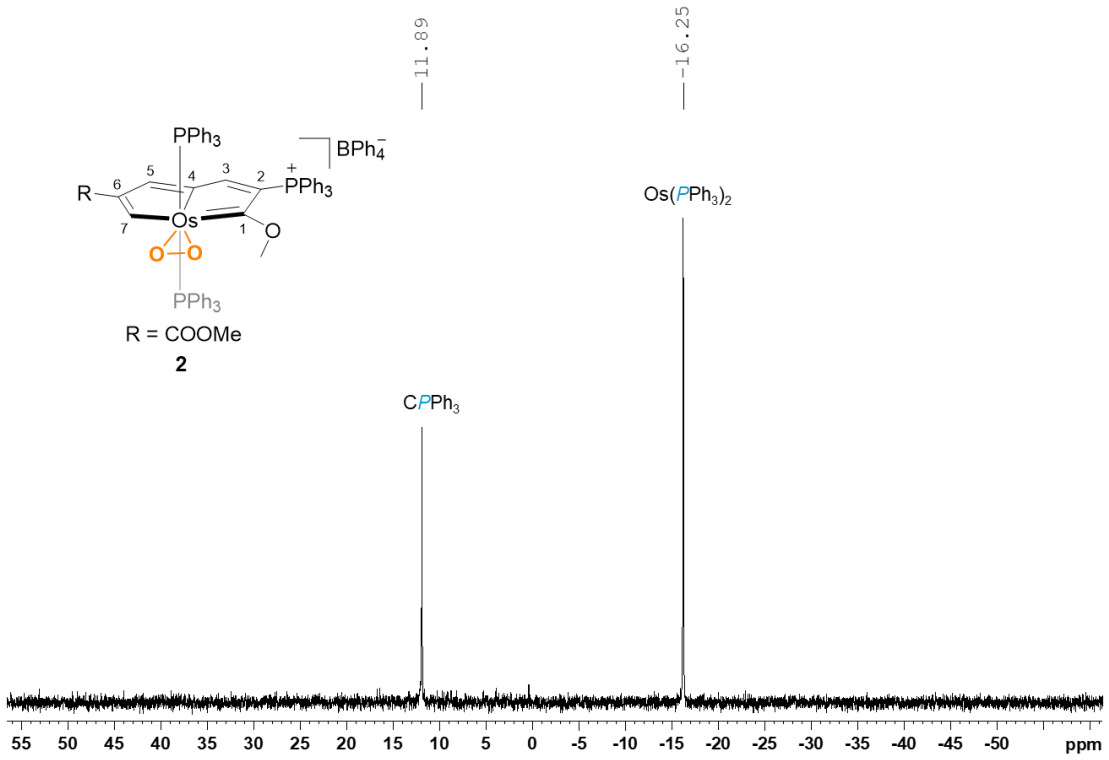

Figure S15. The $^{31}P\{^{1}H\}$ NMR (162.0 MHz, CD_2Cl_2) spectrum for complex **2**. Related to Scheme 1.

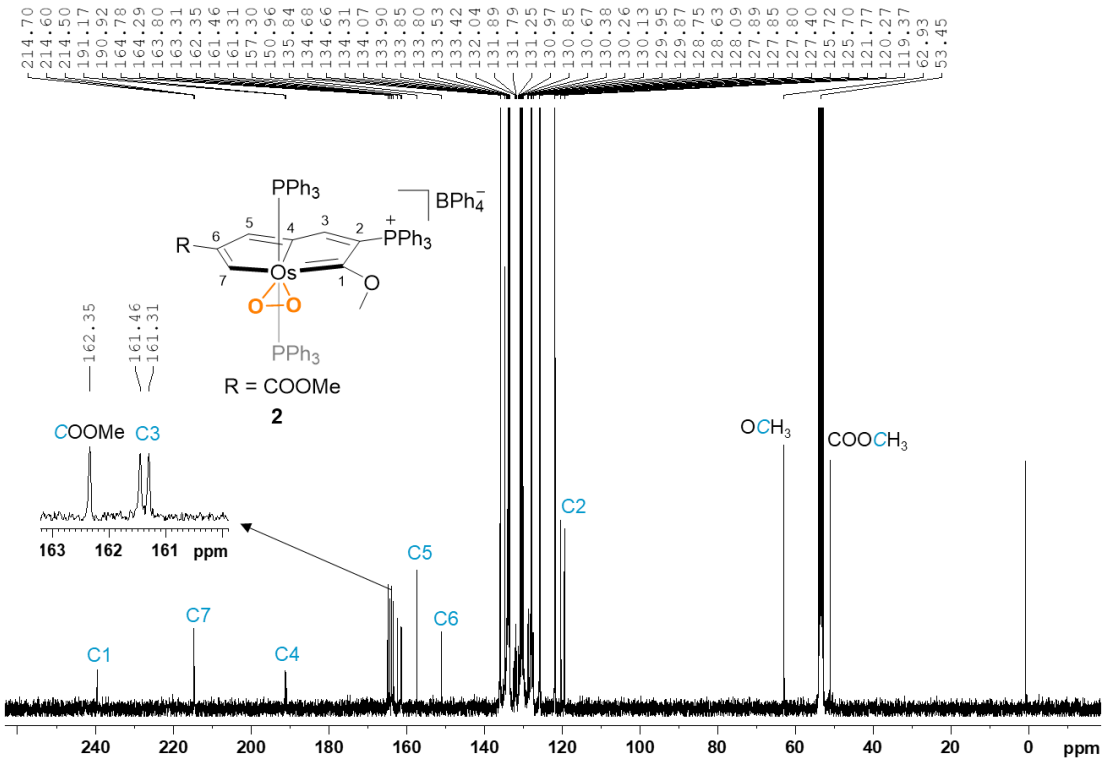

Figure S16. The $^{13}C\{^{1}H\}$ NMR (100.6 MHz, CD_2Cl_2) spectrum for complex **2**. Related to Scheme 1.

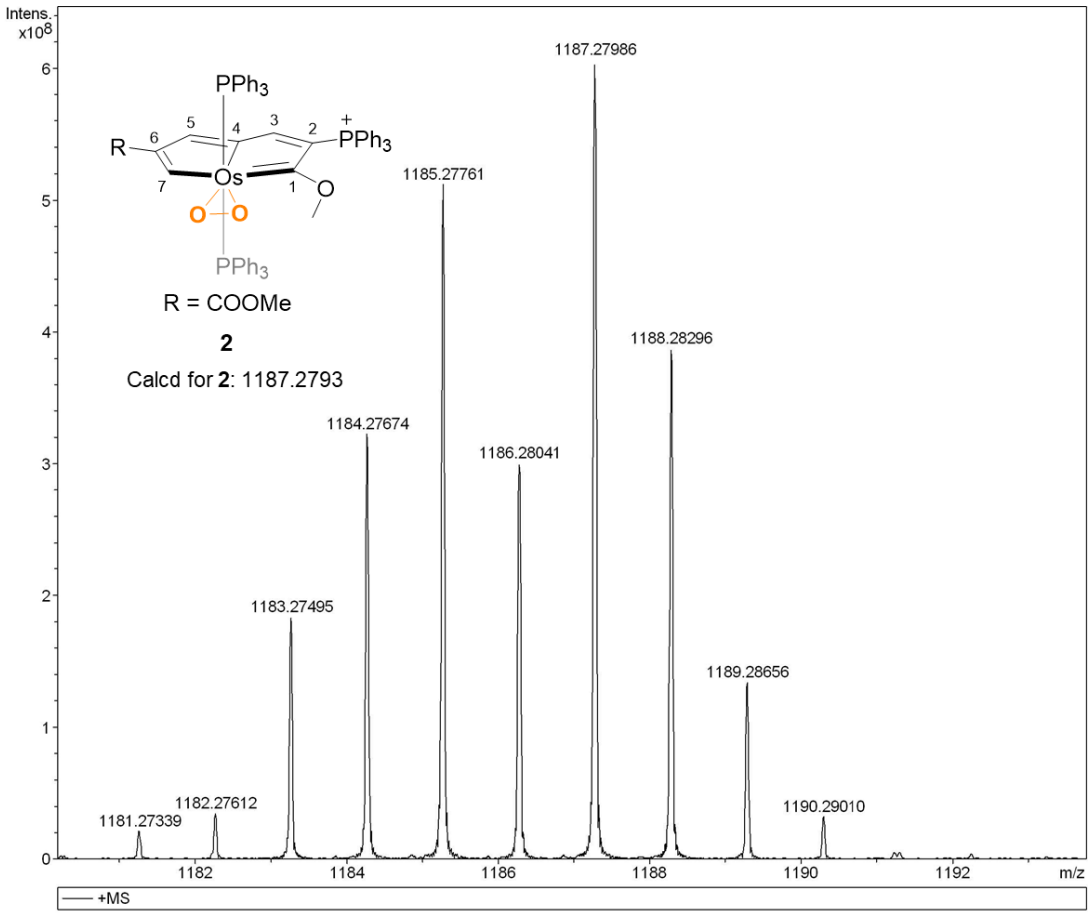

Figure S17. Positive-ion ESI-MS spectrum for complex **2** measured in methanol. Related to Figure 1.

Table S1. Crystal data and structure refinement for **2**. Related to Figure 2.

Empirical formula	$BC_{90}Cl_4H_{78}O_5OsP_3$
Formula weight	1675.24
Temperature/K	176(2)
Crystal system	monoclinic
Space group	$P2_1/n$
a/Å	13.0726(3)
b/Å	23.6457(7)
c/Å	25.5454(8)
α/°	90
β/°	98.734(3)
γ/°	90
Volume/Å^3	7804.8(4)
Z	4
ρ_{calc}g/cm^3	1.426
μ/mm^{-1}	1.886
F(000)	3408.0
Crystal size/mm^3	0.3 × 0.2 × 0.2
Radiation	MoKα (λ = 0.71073)
2Θ range for data collection/°	4.13 to 49.998
Index ranges	$-15 \leq h \leq 15$, $-28 \leq k \leq 28$, $-30 \leq l \leq 30$
Reflections collected	36994
Independent reflections	13735 [R_{int} = 0.0745, R_{sigma} = 0.1006]
Data/restraints/parameters	13735/60/895
Goodness-of-fit on F^2	0.999
Final R indexes [I>=2σ (I)]	R_1 = 0.0556, wR_2 = 0.0963
Final R indexes [all data]	R_1 = 0.0844, wR_2 = 0.1049
Largest diff. peak/hole / e Å^{-3}	1.42/-0.68

Transparent Methods

General Information. Unless otherwise stated, all manipulations were carried out under an inert atmosphere (N_2) using standard Schlenk techniques or a glovebox. Nitrogen was purified by passing through columns of supported P_2O_5. Solvents were distilled from sodium/benzophenone (hexane and diethyl ether) or calcium hydride (dichloromethane and 1,2-Dichlorethane) under N_2 prior to use. $H_2{}^{18}O$ (90% ^{18}O-enriched) was purchased from *J&K* Scientific company. $^{18}O_2$ (97% ^{18}O-enriched) and D_2O (99% D-enriched) were purchased from Sigma-Aldrich company. The metallopentalyne were synthesized according to previously published procedures (Zhu et al., 2013). All other reagents were used as received from commercial sources without further purification. Column chromatography was performed on silica gel (200-300 mesh) in air. NMR spectroscopic experimentals was recorded using a Bruker Advance II 400 spectrometer (^1H, 400.1 MHz; ^{13}C, 100.6 MHz; ^{31}P, 162.0 MHz), a Bruker Advance III 500 spectrometer (^1H, 500.2 MHz; ^{13}C, 125.8 MHz; ^{31}P, 202.5 MHz) or a Bruker Ascend III 600 spectrometer (^1H, 600.1 MHz; ^{13}C, 150.9 MHz; ^{31}P, 242.9 MHz) at room temperature. The ^1H and ^{13}C NMR chemical shifts (δ) are relative to tetramethylsilane, and the ^{31}P NMR chemical shifts are relative to 85% H_3PO_4. The absolute values of the coupling constants are given in hertz (Hz). Two-dimensional and one-dimensional NMR are abbreviated as heteronuclear single quantum coherence (HSQC), heteronuclear multiple bond correlation (HMBC), and distortionless enhancement by polarization transfer (DEPT). The multiplicities are abbreviated as s (singlet), d (doublet), t (triplet), q (quartet), m (multiplet), and br (broad). High-resolution mass spectrometry (HRMS) was conducted using a Bruker En Apex-Ultra 7.0 T FT-MS instrument. GC analysis was performed on a GC-2060 spectrometer or a SHIMADZU QP-2010 Plus GC-MS spectrometer Infrared spectra were obtained using a Nicolet AVATAR FTIR380 spectrometer using KBr discs.

Single-Crystal X-Ray Diffraction Experiments. Single-crystal X-ray diffraction data were collected on an Agilent SuperNova Dual system with mirror-monochromated Mo Kα radiation (λ = 0.71073 Å). A multi-scan absorption correction was performed using

CrysAlisPro 1.171.38.43 (CrysAlisPro Software System, Rigaku Oxford Diffraction, 2015) using spherical harmonicsas implemented in SCALE3 ABSPACK. The structure was solved with the ShelXT (Sheldrick, 2015) structure solution program using the Intrinsic Phasing solution method and by using Olex2 (Dolomanov et al., 2009) as the graphical interface. The model was refined with version 2016/6 of ShelXL (Sheldrick, 2015) using Least Squares minimisation. Non-H atoms were refined anisotropically unless otherwise stated. The hydrogen atoms were introduced at their geometric positions and refined as riding atoms unless otherwise stated. Single crystals suitable for X-ray diffraction were grown from a solution of CH_2Cl_2 layered with hexane. The solvent molecules, dichloromethane, in **2** were masked due to the disorder. Methoxycarbonyl group in **2** was disordered and refined with suitable restraints. Deposition Number CCDC 1892835 for **2** contain the supplemental crystallographic data for this paper. These data are provided free of charge by the joint Cambridge Crystallographic Data Centre and Fachinformationszentrum Karlsruhe Access Structures service www.ccdc.cam.ac.uk/structures. Further details on the crystal data, data collection, and refinements are provided in Table S1. Related to Figure 2.

Computational Details. Related to Figures 3, 5 and 6.

ASE calculations: Structures were optimized at the M06L functional (Lee et al., 1988; Miehlich et al., 1989; Becke, 1993) with the Gaussian 09 software package (Frisch et al., 2009). Frequency calculations were performed to confirm that the optimized geometries were minima on the potential energy surface. The SDD (Dunning and Hay, 1977) pseudo potentials were used for the Os and P atoms, whereas the standard 6-31G* basis set was used for the C, O, and H atoms. Polarization functions were added for Os (ζ(f) = 0.886) and P (ζ(d) = 0.340) (Huzinaga, 1985) in calculations.

NICS and ACID calculations: Structures were first optimized at the B3LYP/6-31G* functional with the Gaussian 09 software package. The LanL2DZ (Hay and Wadt, 1985) pseudo potentials were used for the Os and P atoms, with polarization functions added for Os (ζ(f) = 0.886) and P (ζ(d) = 0.340) in calculations.

The standard 6-311++G** basis set was used for the C, O, and H atoms in the NICS

(Schleyer et al., 1996; Chen et al., 2005; Fallah-Bagher-Shaidaei et al., 2006) and ACID calculations. The anisotropy of the current-induced density (ACID) calculations were carried out with the ACID program (Herges and Geuenich, 2001; Geuenich et al., 2005).

Reaction mechanism calculations: Structure optimizations were carried out by using B3LYP functional as implemented in the Gaussian 09 program. The effective core potentials (ECPs) given by Hay and Wadt with a double-ζ valence basis set (LanL2DZ) were used to describe the Os atom, while the standard 6-31G* basis set was used for C, H, O and P atoms. The energies were further refined using a mixed basis set (LANL2TZ(f) for Os and 6-311G** for the rest atoms). During all calculations, the self-consistent reaction field (SCRF) method (SCRF = SMD) (Marenich et al., 2009) was used to treat the solvent effect of Dichloromethane (ε = 8.93).

Preparation and characterization of osmium-peroxo species 2. Related to Scheme 1 and Figure 1.

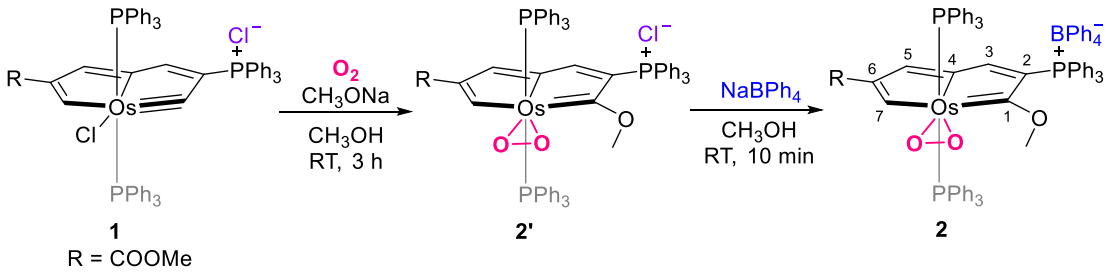

Figure S18. The synthetic route of **2**. Related to Scheme 1.

Osmapentalyne **1** (1.19 g, 1 mmol), CH_3ONa (270 mg, 5 mmol) were placed in a Shlenk flask (100 mL). Under an O_2 atmosphere, methanol (30 mL) was injected *via* syringe, and then the reaction mixture was stirred at ambient temperature for 3 h when the ^{31}P NMR spectra of the reaction mixture indicated that the starting material had been completely converted to **2′** (^{31}P-NMR (162.0 MHz, CD_2Cl_2): δ = 11.83 (s, C*P*Ph_3), −16.23 ppm (s, Os*P*Ph_3). HRMS (ESI): *m/z* calcd for $[C_{64}H_{54}O_5OsP_3]^+$, 1187.2793; found, 1187.2762). Then $NaBPh_4$ (1.71 g, 5 mmol) was slowly added into the mixture, giving a precipitate, which was collected and washed with water, methanol and diethyl ether separately. The solvent was dried under vacuum to give **2** as a brown solid (1.23 g, 82% yield).

^1H NMR (400.1 MHz, CD_2Cl_2): δ (ppm) = 13.17 (q, $J_{P\text{-}H}$ = 3.0 Hz, 1H, H7), 8.70 (d, $J_{P\text{-}H}$ = 3.2 Hz, 1H, H5), 8.38 (d, $J_{P\text{-}H}$ = 5.8 Hz, 1H, H3), 3.92 (s, 3H, OC*H*$_3$), 3.55 (s, 3H, COOC*H*$_3$), 7.77-6.86 (m, 45H, PPh_3). ^{31}P NMR (162.0 MHz, CD_2Cl_2): δ (ppm)= 11.89 (s, C*P*Ph_3), −16.25 (s, Os*P*Ph_3). ^{13}C NMR (100.6 MHz, CD_2Cl_2): δ (ppm) = 239.52 (t, $J_{P\text{-}C}$ = 8.1 Hz, C1), 214.60 (t, $J_{P\text{-}C}$ = 9.6 Hz, C7), 191.05 (d, $J_{P\text{-}C}$ = 24.4 Hz, C4), 162.35(s, *C*$OOCH_3$) 161.38 (d, $J_{P\text{-}C}$ = 15.5 Hz, C3), 157.30 (s, C5), 119.81 (d, $J_{P\text{-}C}$ = 90.0 Hz, C2), 150.96 (s, C6), 62.93 (s, O*C*H_3), 51.09 (s, COO*C*H_3), 119.37-135.84 (m, PPh_3). HRMS (ESI): *m/z* calcd for $[C_{64}H_{54}O_5OsP_3]^+$, 1187.2793; found, 1187.2798.

Supplemental references

Zhu, C., Li, S., Luo, M., Zhou, X., Niu, Y., Lin, M., Zhu, J., Cao, Z., Lu, X., Wen, T., et al. (2013). Stabilization of anti-aromatic and strained five-membered rings with a transition metal. Nat. Chem. *5*, 698-703.

CrysAlisPro Software System, Rigaku Oxford Diffraction, (2015).

Sheldrick, G. M. (2015). ShelXT-Integrated space-group and crystal-structure determination, Acta Crystallographica, *A71*, 3-8.

Dolomanov, O.V., Bourhis, L.J., Gildea, R.J., Howard, J.A.K., and Puschmann, H. (2009). OLEX2: a complete structure solution, refinement and analysis program. Journal of Applied Crystallography *42*, 339-341.

Sheldrick, G. M. (2015). Crystal structure refinement with SHELXL. Acta Crystallographica, *C27*, 3-8.

Lee, C., Yang, W., and Parr, R.G. (1988). Development of the Colle-Salvetti correlation-energy formula into a functional of the electron density. Physical Review B *37*, 785-789.

Miehlich, B., Savin, A., Stoll, H., and Preuss, H. (1989). Results obtained with the correlation energy density functionals of becke and Lee, Yang and Parr. Chemical Physics Letters *157*, 200-206.

Becke, A.D. (1993). Density‐functional thermochemistry. III. The role of exact exchange. The Journal of Chemical Physics *98*, 5648-5652.

Frisch, M.J., Trucks, G., Schlegel, H.B., Scuseria, G.E., Robb, M.A., Cheeseman, J., Scalmani, G., Barone, V., Mennucci, B., Petersson, G.A., et al. (2009). Gaussian 09 Revision A.1. Gaussian Inc.

Dunning, J.T.H., Hay, P. J. (1977). In Modern Theoretical Chemistry, H.F. Schaefer, ed. (New York: Plenum), pp. 1-28.

Huzinaga, S. (1985). Basis sets for molecular calculations. Computer Physics Reports *2*, 281-339.

Hay, P.J., and Wadt, W.R. (1985). Ab initio effective core potentials for molecular calculations. Potentials for K to Au including the outermost core orbitals. The Journal of Chemical Physics *82*, 299-310.

Schleyer, P.v.R., Maerker, C., Dransfeld, A., Jiao, H., and van Eikema Hommes, N.J.R. (1996). Nucleus-Independent Chemical Shifts: A Simple and Efficient Aromaticity Probe. J. Am. Chem. Soc. *118*, 6317-6318.

Chen, Z., Wannere, C.S., Corminboeuf, C., Puchta, R., and Schleyer, P.v.R. (2005). Nucleus-Independent Chemical Shifts (NICS) as an Aromaticity Criterion. Chem. Rev. *105*, 3842-3888.

Fallah-Bagher-Shaidaei, H., Wannere, C.S., Corminboeuf, C., Puchta, R., and Schleyer, P.v.R. (2006). Which NICS Aromaticity Index for Planar π Rings Is Best? Org. Lett. *8*, 863-866.

Herges, R., and Geuenich, D. (2001). Delocalization of Electrons in Molecules. J. Phys. Chem. A *105*, 3214-3220.

Geuenich, D., Hess, K., Köhler, F., and Herges, R. (2005). Anisotropy of the Induced Current Density (ACID), a General Method To Quantify and Visualize Electronic Delocalization. Chem. Rev. *105*, 3758-3772.

Marenich, A.V., Cramer, C.J., and Truhlar, D.G. (2009). Universal Solvation Model Based on Solute Electron Density and on a Continuum Model of the Solvent Defined by the Bulk Dielectric Constant and Atomic Surface Tensions.

The Journal of Physical Chemistry B *113*, 6378-6396.